Submitted to Structures

Two-step parameter identification of multi-axial cyclic constitutive law of structural steels from cyclic structural responses

Makoto Ohsaki[a], Bach Do[a,*], Jun Fujiwara[b], Toshiaki Kimura[c], Takuzo Yamashita[d]

[a]*Department of Architecture and Architectural Engineering, Graduate School of Engineering, Kyoto University, Kyoto 615-8540, Japan*
[b]*Earthquake Disaster Mitigation Research Division, National Research Institute for Earth Science and Disaster Resilience, Miki 673-0515, Japan*
[c]*Graduate School of Design and Architecture, Nagoya City University, Nagoya 464-0083, Japan*
[d]*Earthquake Disaster Mitigation Research Division, National Research Institute for Earth Science and Disaster Resilience, Tsukuba 305-0006, Japan*

Abstract

This paper presents a two-step Bayesian optimization (BO) method for identifying the elastoplastic material parameters of structural steels subjected to multi-axial cyclic loading. A series of simple elastic and elastoplastic shaking table tests is conducted for a structure that has a steel specimen experiencing elastoplastic response. An inverse problem is formulated to identify the multi-axial material parameters of the specimen from the structural responses obtained by the shaking table tests. This is notable because it is more difficult to carry out multi-axial static cyclic material tests than to conduct dynamic cyclic structural tests. The inverse problem minimizes the error between the measured structural responses and those simulated by finite element (FE) analysis. The two-step BO devised for solving the inverse problem successfully offers a global optimization framework while considerably reducing the number of costly simulations. It first seeks to infer Young's modulus values from the cyclic elastic responses of the structure, thereby validating the FE model in its elastic state. It then finds the parameters for the nonlinear combined isotropic/kinematic hardening model of the specimen using the cyclic elastoplastic responses of the structure. Verification results show that the parameters identified by the proposed method well reproduce the cyclic responses of the structure under different cyclic loading conditions.

Keywords: Multi-axial constitutive law, Cyclic loading, Parameter identification, Structural steels, Bayesian optimization.

1. Introduction

Modeling the cyclic constitutive law of structural steels for an elastoplastic finite element (FE) analysis plays an important role in detailed evaluation of seismic responses of steel structures. By combining a proper constitutive law with suitable structural elements for plastic behavior, FE analysis has successfully provided accurate responses of structural members, for example, steel hollow-section columns [1] and steel end-plate connections [2] subjected to cyclic deformation. Residual stresses at welds can also be precisely evaluated [3], and detailed seismic responses of medium and super-high-rise steel buildings are obtained [4, 5] even though they are designed using frame models. It is obvious that selecting an appropriate constitutive law is important to ensure the accuracy of obtained response analysis. Many studies, therefore, have been dedicated to construction of different constitutive models addressing various aspects of cyclic elastoplastic deformations, for example, the behavior of different steel grades [6], the cyclic hardening and softening behavior [7], the yield plateau [8, 9], a decrease in yield stress [10], the Bauschinger and ratcheting effects [11, 12], and the effects of strain rates and temperatures [13] on the steel behavior.

In the structural engineering field, cyclic elastoplastic constitutive models for structural steels are often defined by several parameters. An inverse problem seeks to infer these parameters by minimizing the error between the experimental and numerical results. Most of the inverse problems, however, have been formulated based on the results of uni-axial cyclic loading tests [6, 8, 14–16]. Although the parameters identified from such experimental results can simulate the behavior of structural components through a continuum plasticity model, they may not accurately describe the cyclic behavior under a multi-axial loading, for example, a structural member subjected to multi-directional seismic motions, because the hardening behavior of a material depends on the loading history [17]. Thus, it is desirable to identify the elastoplastic parameters from the multi-axial cyclic test. However, it is difficult to carry out a static cyclic material test in

*Corresponding author
Email addresses: ohsaki@archi.kyoto-u.ac.jp (Makoto Ohsaki), se.do@archi.kyoto-u.ac.jp (Bach Do)

multi-axial state. This also motivates the development of an experiment in which an expected cyclic loading condition can be generated for the elastoplastic specimen of a structure, and the structural responses under such a loading condition can be measured to formulate a more reliable inverse problem.

Methods for solving inverse parameter identification problems can be categorized into probabilistic and deterministic approaches. The probabilistic approach [18–21] relies on Bayesian updating to handle uncertainties in the material parameters that are inherent and/or caused by noise involved in the properties of specimen and measurements of experimental response. Bayes' rule updates a prior probability density function (PDF) for each material parameter, specified by the user, based on a likelihood function that is a joint density function of the measured responses and the parameters. Once implemented, the probabilistic approach offers a posterior PDF for each parameter from which the samples for each parameter can be generated using a posterior sampling technique such as Markov chain Monte Carlo method [22]. Using the generated samples, each parameter can be estimated statistically and further used as input to other FE analyses. A key issue of the probabilistic approach is that it is difficult to find a proper likelihood function because it is commonly not available in an analytical form or it is too expensive to evaluate [23]. Also, structural engineers still hesitate to perform sophisticated probabilistic computations in practice [24].

The deterministic approach that offers an estimate for each material parameter [9, 16, 24–29] is commonly adopted in engineering practice because its underlying mathematics is simple and easy to understand. The approach minimizes an error function describing the difference between the experimental data and numerical predictions. Regularization methods [30, 31], for example, generalized Tikhonov, weighting Tikhonov, or total variational regularization, may be used to handle the ill-posed nature of inverse problems by adding penalty terms to the error function. The deterministic approach solves the inverse problem using an optimization algorithm selected among population-based [27, 32], gradient-based [28], and hybrid algorithms [26]. The selection of a proper optimization algorithm depends on the characteristic of the error function, for example, cheap-to-evaluate or costly-to-evaluate. Since modeling the uni-axial elastoplastic behavior of structural steels does not arise major computational issue, any optimization algorithms can be used for solving the associated inverse problem. However, the optimization algorithm should be carefully selected for solving the inverse problem formulated from the elastoplastic responses of a structure subjected to multi-axial cyclic loading with a large number of cycles because the associated simulation demands a substantial computational cost.

With the rise of computational power and notable advances in machine learning methods in recent years, the data-driven approach to constructing data-based material models without using any classical constitutive law has become an active field in mechanics and materials science [33]. This approach is able to solve inverse problems deterministically as well as probabilistically [34]. However, its application to cyclic constitutive modeling for structural steels is still rare because the available experimental data from cyclic tests of steel specimens, steel members, and steel structures are relatively limited to provide meaningful data for a data-driven approach.

This study presents an experimental program in which a steel specimen is designed as the only member of a structure that experiences elastoplastic behavior when the structure is subjected to multi-directional dynamic cyclic loading. Thus, the parameters for elastoplastic material property under multi-axial cyclic loading can be identified through the measured structural responses. This is notable because it is more difficult to carry out static cyclic material tests than to conduct dynamic cyclic structural tests. Complex loading equipment and supporting parts are needed for multi-axial static tests. It is also difficult to prevent instability and out-of-plane displacements of specimen during cyclic elastoplastic deformation.

Two main contributions of this study are the innovative experimental program and the identification approach to calibrating the elastoplastic material parameters of structural steels under multi-axial cyclic loading conditions. In particular, multi-axial cyclic elastoplastic deformation is realized in a specimen attached to a simple elastic frame in the shaking table test. A detailed FE model of the experimental structure is developed for identification using responses under various loading conditions that are obtained by simply replacing the specimen and applying different input waves to the actuators. The FE model incorporates the nonlinear combined isotropic/kinematic hardening and linear elastic material models, respectively, to simulate the behaviors of the specimen and other members of the structure, and the elastic and plastic material properties are identified by two identification steps. First, Young's modulus values are found based on the cyclic elastic dynamic responses of the structure. This is to validate the FE model in the elastic state before it is used for carrying out costly cyclic dynamic elastoplastic simulations. Second, the plastic parameters for the nonlinear combined isotropic/kinematic hardening model are identified based on the cyclic elastoplastic responses of the structure. To further address the computational cost of modeling the structure, the inverse problem associated with each identification step is solved using Bayesian optimization (BO) [35–37], thereby requiring two-step BO for identification of all material parameters. Finally, the prediction performance of identified parameters is verified by simulating the experimental results with various cyclic dynamic loading conditions that are not used for identification.

The remainder of this paper is organized as follows. Section 2 briefly describes the experimental program that consists of a series of cyclic dynamic tests and three monotonic tension tests. The FE model of the experiment is detailed in Section 3. Section 4 formulates the two-step identification problem and explains the solution process using BO. Identification and verification results are provided in Section 5. Section 6 summarizes and concludes this paper. Appendices A and B, respectively, describe the nonlinear combined isotropic/kinematic hardening model and the Gaussian process modeling – a key ingredient of BO.

2. Experimental program

2.1. Cyclic dynamic tests

Consider a small steel frame that is a structure for cyclic dynamic tests carried out on a shaking table. A "specimen" that exhibits elastoplastic deformation is located at the center of the structure shown in Fig. 1. The specimen is carefully designed so that it is the only member of the structure experiencing elastoplastic behavior during a series of shaking table tests. By designing the specimen and the structure in such a way, we can investigate the multi-axial cyclic elastoplastic behavior of the specimen through the measured responses of the structure.

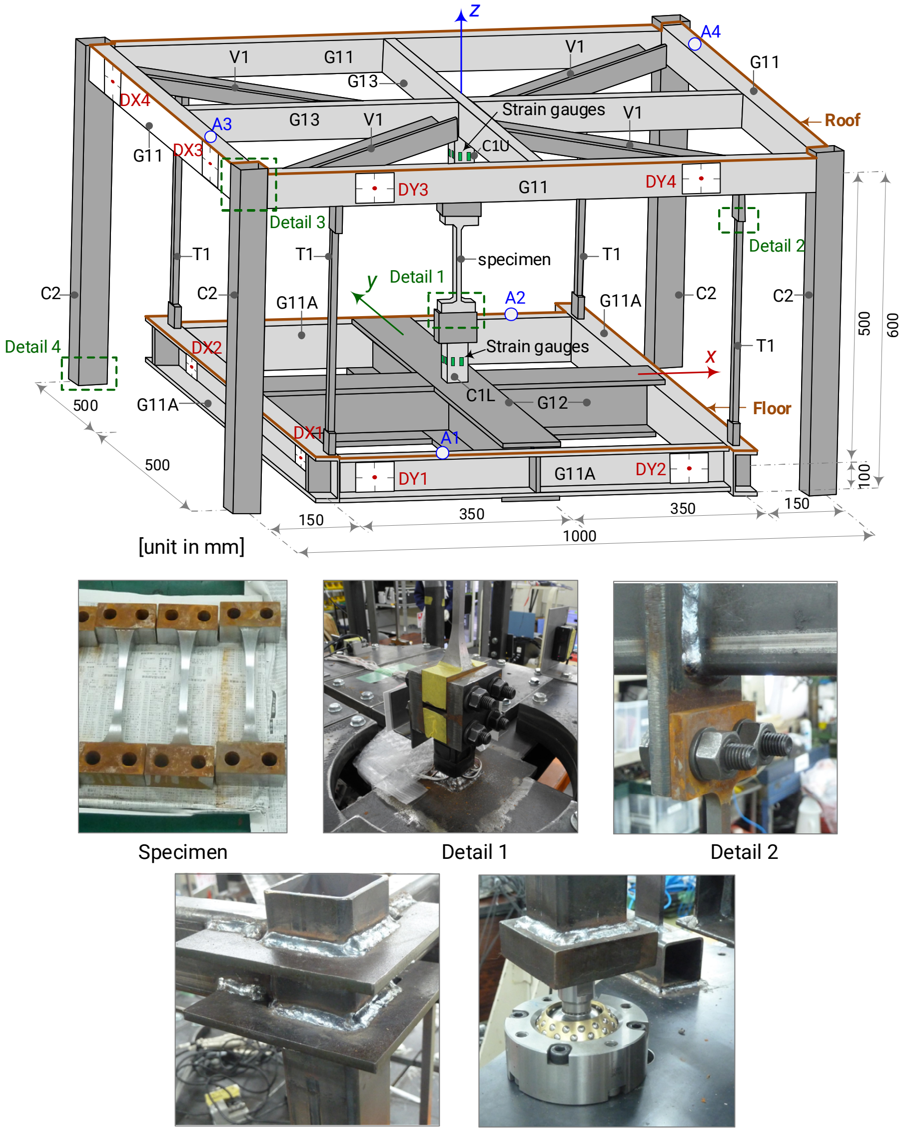

Figure 1: Schematic drawing of the experiment and some connection details.

In the experimental setup, the upper and lower ends of the specimen are rigidly connected to an elastic steel frame (i.e., supporting frame) and a floor, respectively; see Detail 1 in Fig. 1. Four hanging bars T1 connecting the floor and the supporting frame (Detail 2) are made of high-strength steel to ensure their elastic behavior. Four

Table 1: Steel profiles and steel grades for members of the structure.

Member	Profile	Description	Grade
C1L and C1U	SRB $-$ 32×35	Solid rectangular bar	SN490B
C2	SHS $-$ $50 \times 50 \times 3.2$	Square hollow section	STKR400
T1	SSB $-$ 9×9	Solid square bar	HW685
G11	RHS $-$ $60 \times 30 \times 3.2$	Rectangular hollow section	STKR400
G11A	C $-$ $75 \times 40 \times 5 \times 7$	Channel	SS400
G12	I $-$ $100 \times 100 \times 6 \times 8$	Rolled I shape	SS400
G13	FB $-$ 60×16	Flat bar	SS400
V1	EA $-$ $40 \times 40 \times 3$	Equal angle	SS400

perimeter beams G11 of the roof are fixed to four columns C2 of the supporting frame through exterior diaphragm plates and welded connections (Detail 3). The column bases are connected to the shaking table by spherical bearings (Detail 4) that permit three axial rotations by using rolling elements at the contact surface. Two I beams G12 of the floor are welded to each other at their intersection and are connected to four C beams G11A through fin plate connections. The steel profiles and steel grades for the members of the floor, supporting frame, and four hanging bars are given in Table 1, where the steel grades are in accordance with Japanese industrial standards for rolled structural steels for building and general structures (JIS G 3136-SN490B and JIS G 3101-SS400), for carbon steel tubes (JIS G 3466-STKR400), and for weldable high-strength steels (WES 3001-HW685). The material of specimen is JIS G 3101-SS400.

Eighteen steel plates of thickness 25 mm are bolted on the floor. The distribution of steel plates shown in Fig. 2(a) is asymmetric with respect to xz-plane and symmetric with respect to yz-plane, and is the same for all cyclic tests. Therefore, the x-direction (x-dir.) excitation triggers a torsional vibration, while the y-dir. excitation causes no torsional vibration.

The three lowest natural frequencies measured by white noise input with small amplitude are 4.79 Hz (x-dir. and z-rot.), 6.70 Hz (x-dir. and z-rot.), and 7.10 Hz (y-dir.), where rot. is the abbreviation of rotation, i.e., the 1st and 2nd modes are combined modes of translation and torsion.

We carried out a total of 21 cyclic dynamic tests using an electro-hydraulic servo-controlled shaking table that can generate 3-axial displacements and rotations, i.e., 6-degree-of-freedom input motion. The difference between these tests lies in the directions, frequencies, and amplitudes of dynamic waves generated by actuators. Among 21 waves, the 9 waves listed in Table 2 are used for identification, where Type 1 has the maximum acceleration during 10 seconds; Type 2 gradually increases the amplitude from 80% to 100% during the period of 10 seconds. Although the feedback controller is equipped in the actuators of the shaking table, an inevitable error exists between the target and actual displacements of the table. In the following identification, therefore, the table accelerations are measured and regarded as the input accelerations to the numerical model.

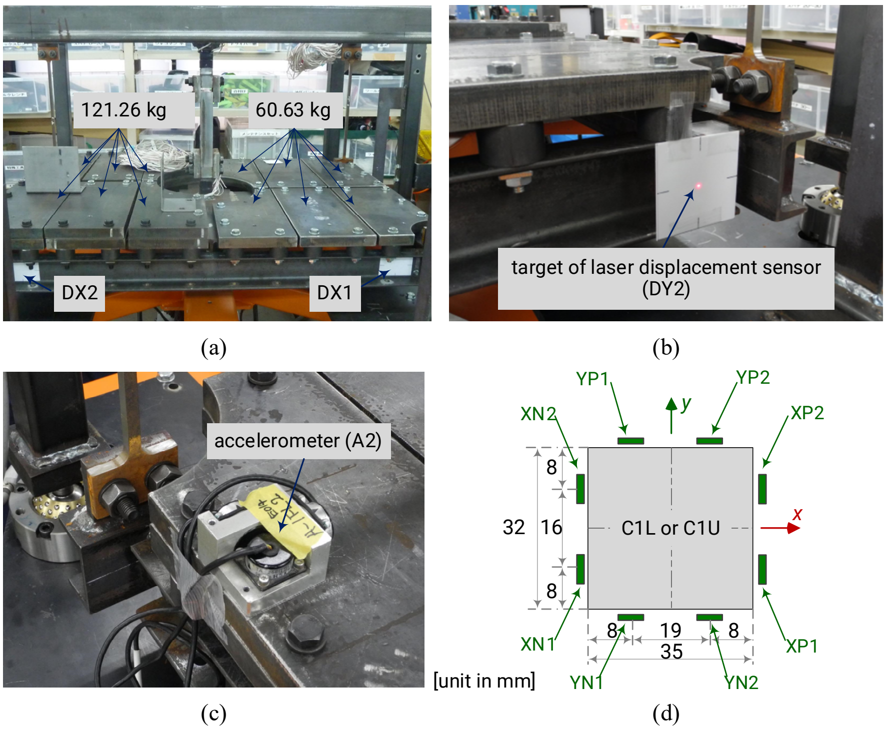

Figure 2: Arrangements of mass and measurement devices. (a) Arrangement of steel plate masses on the floor; (b) A target of a laser displacement sensor; (c) An accelerometer installed; (d) Layout and label of strain gauges at C1L and C1U columns.

Table 2: Dynamic waves generated for the cyclic tests.

Wave ID	Frequency (Hz)			Amplitude (m/s^2)			Type
	$x-$dir.	$y-$dir.	$z-$dir.	$x-$dir.	$y-$dir.	$z-$dir.	
1	–	4.5	–	–	4.52	–	1
2	4.5	6.0	–	4.07	2.41	–	1
3	4.5	6.0	–	4.07	2.41	–	2
4	4.5	–	4.5	3.82	–	5.08	1
5	–	6.0	–	–	4.52	–	1
6	3.5	–	–	4.40	–	–	1
7	3.5	–	3.5	3.96	–	2.68	1
8	–	4.5	4.5	–	4.52	5.42	1
9	4.5	–	4.5	3.82	–	5.08	2

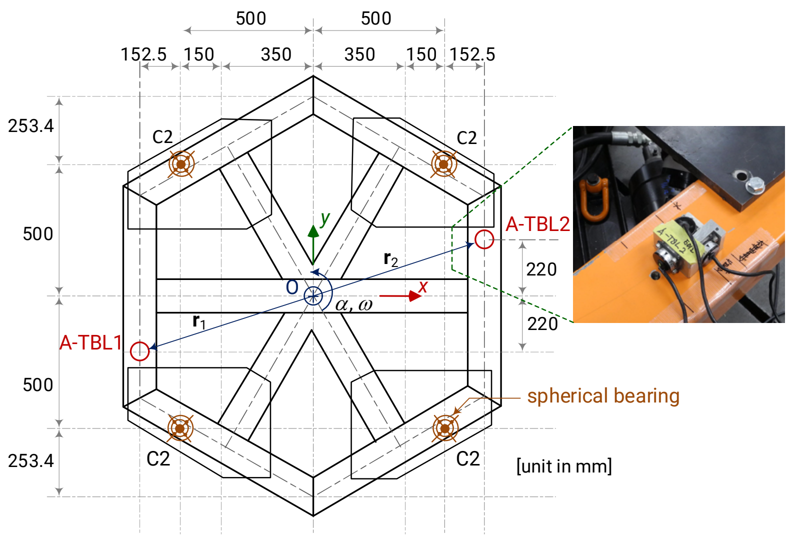

Figure 3: Accelerometers at A-TBL1 and A-TBL2 on the shaking table.

Laser displacement sensors are used to measure the displacements in x- and y-dirs. at the specified locations on the floor and roof of the structure. As indicated in Fig. 1, DX1, DX2, DX3, and DX4 are four locations for measuring x-dir. displacements, and DY1, DY2, DY3, and DY4 for measuring y-dir. displacements. Figure 2(b) shows the target of the laser displacement sensor DY2. To measure the accelerations of interest in x-, y-, and z-dirs., a total of six servo-type tri-axis accelerometers are installed at two locations A1 and A2 on the floor (i.e., on the steel plate masses), two locations A3 and A4 on the roof (see Fig. 1), and two locations A-TBL1 and A-TBL2 on the shaking table (see Fig. 3). Figures 2(c) and 3 show the photos of the accelerometers at A2 and A-TBL2, respectively. Moreover, a total of 16 strain gauges are attached at two sections of short columns C1L and C1U supporting the lower and upper ends of the specimen, respectively, to measure the axial strains on four sides of each section. From the measured axial strains, the bending moments at C1L and C1U are calculated as detailed in Section 4. The labels of eight strain gauges at each section and their layout are detailed in Fig. 2(d).

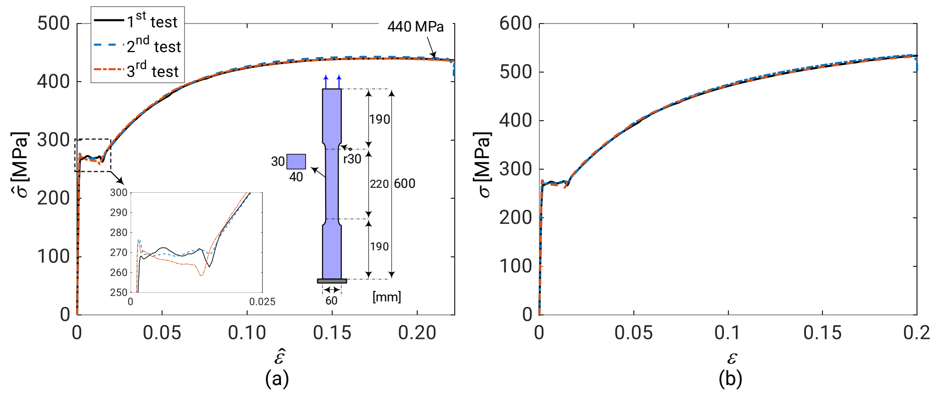

Figure 4: Geometric property of the rods used in three monotonic tension tests and stress–strain curves obtained from these tests. (a) engineering stress–strain; (b) true stress–strain.

2.2. Monotonic tension tests

To facilitate the determination of Young's modulus E and the initial yield stress $\sigma_{\mathrm{y},0}$ for the material model of the specimen, we also conducted monotonic tension tests on three rods extracted from the same lot of the specimen used in the cyclic tests. The testing and measurements of mechanical characteristics are according to JIS Z 2241. Figure 4 shows the geometric property of the rod and the relation between the engineering stress $\hat{\sigma}$ and engineering strain $\hat{\epsilon}$ obtained from the monotonic tension tests. The true stress σ and true strain ϵ are also derived from $\hat{\sigma}$ and $\hat{\epsilon}$. The three $\hat{\sigma} - \hat{\epsilon}$ (or $\sigma - \epsilon$) curves are almost identical and each has an obvious yield plateau. The monotonic hardening process shows the feature of a nonlinear function, which can facilitate the selection of a nonlinear hardening model. Young's modulus values obtained from the first, second, and third monotonic tension tests are 208.01, 207.15, and 204.17 GPa, respectively, and the corresponding initial yield stress values are 268.22, 276.86, and 275.38 MPa. The ultimate stress is about 440 MPa for the three tests, roughly 1.6 times the initial yield stress, and the ratio of the strain at ultimate stress to the yield strain is roughly 150.

3. Numerical simulation

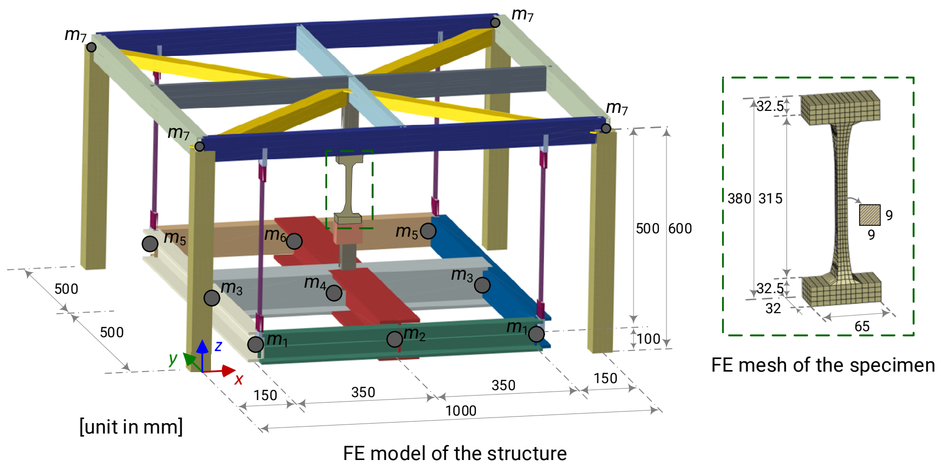

Figure 5: FE model of the structure and FE mesh of the specimen.

All simulations are performed using Abaqus 2020 [38]. The FE model of the structure and the mesh of the specimen are shown in Fig. 5. The members of the structure, except the specimen, are modeled using beam elements of type B31. Bending moments are fully-released at the ends of several beam elements connected by bolted connections, for example, two ends of brace V1 on the roof. This, however, is not applicable to the beams on the floor because the end rotations of these beams are restrained by the rigid steel plates. To reduce the sensitivity of simulation results to the FE mesh density, we generate a fine mesh consisting of 1440 eight-node linear-brick elements of type C3D8, 128 six-node wedge elements of type C3D6, and 2215 nodes for modeling the specimen. Column C2 and hanging bar T1 are modeled by three and four beam elements along their axis, respectively. In addition, concentrated masses, as detailed in Fig. 5, are assigned at

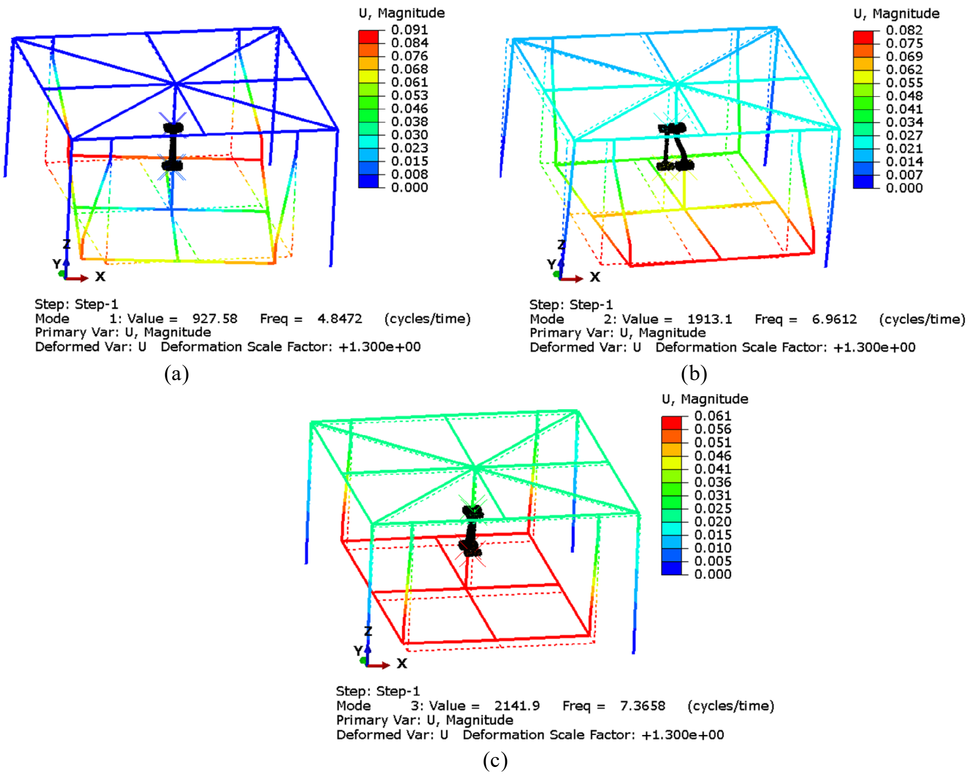

Figure 6: First three mode shapes of the structure for $E = 205$ and $E_1 = E_2 = E_3 = 200$ GPa. (a) 1st mode; (b) 2nd mode; (b) 3rd mode.

nine nodes on the floor (i.e., $m_1 \times 2$, m_2, $m_3 \times 2$, m_4, $m_5 \times 2$, and m_6) and four nodes on the roof (i.e., $m_7 \times 4$). The values of $m_1, m_2, \ldots, m_7$ are 8.92, 22.84, 29.46, 39.27, 13.75, 43.58, 1.00 (kg), respectively. Note that the concentrated masses on the floor include the total mass of the steel plates, measurement devices, and spacers, and those on the roof are from the masses of the exterior diaphragm plates of Detail 3 in Fig. 1.

To further incorporate the mass from connection bolts and stiffeners on the floor, we assign the mass density of the floor beams as 7870 kg/m^3 instead of 7860 kg/m^3 for other members. Poisson's ratio is 0.3 for all steels of the structure. The material behavior of the specimen is simulated using the nonlinear combined isotropic/kinematic hardening model as described in Appendix A, which allows an exponential hardening law. Such a hardening model, when using only one back-stress component and a specified value of Poisson's ratio, is parameterized by six parameters, namely, Young's modulus E, initial yield stress $\sigma_{\mathrm{y},0}$, isotropic hardening parameters Q_∞ and b, and nonlinear kinematic hardening parameters C_1 and γ_1. Also, the linear elastic material model parameterized by Young's modulus is used for simulating the material behavior of beams and columns. Since the monotonic tension tests for materials of beams and columns are not available, we first assign E, E_1, E_2, and E_3 as Young's modulus values for columns C1L and C1U, columns C2 and beams on the roof, beams on the floor, and hanging bars, respectively. Note that the same value E as the specimen is assumed for columns C1L and C1U, because they are serially connected to the specimen, and it is difficult to distinguish the elastic properties of specimen and column in the identification process. We then identify them based on the cyclic elastic behavior of the structure in the first identification step.

To take into account gravity, the stress field for gravity is computed before performing dynamic analysis. The first three mode shapes of the structure corresponding to $E = 205$ and $E_1 = E_2 = E_3 = 200$ GPa are depicted in Fig. 6. Similar to the experimental results, x-dir. displacement and torsion around z-axis dominate and interact in modes 1 and 2, while mode 3 corresponds to a y-dir. vibration. The the three lowest frequencies are 4.85, 6.96, and 7.37 (Hz), which are slightly larger than those obtained by the experiment. The Rayleigh damping coefficients are calculated using a 2% damping ratio for the first and third modes of the structure.

The "rigid body" is used to define the kinematic constraints between the specimen and the columns C1U and C1L, respectively. The column bases are modeled as pin joints that are kinematically coupled with a reference node O that is the center of the shaking table as shown in Fig. 3. Here, the shaking table is considered as a rigid body, and its entire motion is governed by the motion of O. Thus, the input accelerations are assigned in the horizontal plane at O of the FE model. The calculation of such input accelerations relies on the acceleration records from the accelerometers at A-TBL1 and A-TBL2, which is detailed as follows.

We decompose the motion of O into translation vector and rotation about the vertical axis. Let $\mathbf{a}_{\mathrm{O}}$, $\mathbf{a}_{\mathrm{TB1}}$, and $\mathbf{a}_{\mathrm{TB2}}$ denote the translational acceleration vectors at O, A-TBL1, and A-TBL2, respectively. Each of these vectors has two components: accelerations a_{x} and a_{y} in x- and y-dirs. Let $\boldsymbol{\alpha} = \alpha\mathbf{k}$ and $\boldsymbol{\omega} = \omega\mathbf{k}$ represent the angular acceleration and angular velocity vectors of the rotation, respectively, where $\mathbf{k}$ is the unit vector in

z-dir. (see Fig. 3), and α and ω take positive values if the rotation is counter-clockwise when viewed from the top. Also, let $\mathbf{r}_1$ and $\mathbf{r}_2$ denote the vectors locating A-TBL1 and A-TBL2 from O, respectively. Kinematics of the rigid shaking table reads

$$\begin{aligned}\mathbf{a}_{\mathrm{TB1}} &= \mathbf{a}_{\mathrm{O}} + \alpha\mathbf{k} \times \mathbf{r}_1 - \omega^2\mathbf{r}_1,\\ \mathbf{a}_{\mathrm{TB2}} &= \mathbf{a}_{\mathrm{O}} + \alpha\mathbf{k} \times \mathbf{r}_2 - \omega^2\mathbf{r}_2.\end{aligned} \tag{1}$$

Thus, we have

$$\mathbf{a}_{\mathrm{TB1}} - \alpha\mathbf{k} \times \mathbf{r}_1 + \omega^2\mathbf{r}_1 = \mathbf{a}_{\mathrm{TB2}} - \alpha\mathbf{k} \times \mathbf{r}_2 + \omega^2\mathbf{r}_2. \tag{2}$$

Projecting Eq. (2) onto x- and y-dirs. leads to a linear system of two equations in two variables α and ω. Since a_{x} and a_{y} components of $\mathbf{a}_{\mathrm{TB1}}$ and $\mathbf{a}_{\mathrm{TB2}}$ are known from the two accelerometers at A-TBL1 and A-TBL2, α and ω can be found easily by solving the linear system. With α and ω, $\mathbf{a}_{\mathrm{O}}$ can be found from Eq. (1). Then, $\mathbf{a}_{\mathrm{O}}$ and α are assigned at O as the input accelerations for the FE model. The maximum increment for each acceleration history is set as 0.01 s.

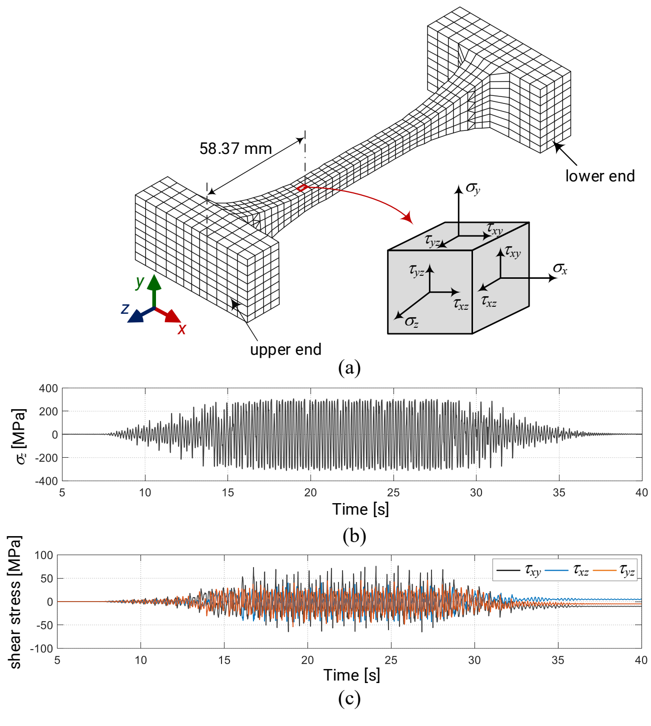

Figure 7: Example of histories of normal and shear stresses at the first integration point of an element of the specimen model. (a) Element of consideration; (b) Normal stress; (c) Shear stresses.

Figure 7 shows an example of histories of normal and shear stresses at the first integration point of an element of the specimen model when the structure is subjected to wave 2 in Table 2 and the material parameters have been identified. The element corresponds to the region where plastic deformations in the specimen occurred. It is confirmed that there is a complex multi-axial stress state in this element and the normal stress (i.e., σ_z) is dominant in this case.

4. Two-step parameter identification

4.1. Responses of interest

The responses of interest are defined for each cyclic test to detect the cyclic hardening process during the test and to formulate the identification problem. Let $(u_{\mathrm{x1}}, u_{\mathrm{x2}}, u_{\mathrm{x3}}, u_{\mathrm{x4}})$ denote the x-dir. displacements measured at locations (DX1, DX2, DX3, DX4), and $(u_{\mathrm{y1}}, u_{\mathrm{y2}}, u_{\mathrm{y3}}, u_{\mathrm{y4}})$ denote the y-dir. displacements at locations (DY1, DY2, DY3, DY4). The relative displacements between the floor and roof in x- and y-dirs. are obtained as

$$\begin{aligned} \delta_{\mathrm{x}} &= \frac{1}{2}(u_{\mathrm{x1}} + u_{\mathrm{x2}} - u_{\mathrm{x3}} - u_{\mathrm{x4}}), \\ \delta_{\mathrm{y}} &= \frac{1}{2}(u_{\mathrm{y1}} + u_{\mathrm{y2}} - u_{\mathrm{y3}} - u_{\mathrm{y4}}). \end{aligned} \tag{3}$$

Let $(\epsilon_{\mathrm{z1}}, \epsilon_{\mathrm{z2}}, \epsilon_{\mathrm{z3}}, \epsilon_{\mathrm{z4}})$ indicate the axial strains measured by the strain gauges (XN1, XN2, XP1, XP2) of column C1L (see Fig. 2(d)), and $(\epsilon_{\mathrm{z5}}, \epsilon_{\mathrm{z6}}, \epsilon_{\mathrm{z7}}, \epsilon_{\mathrm{z8}})$ indicate the axial strains by (YN1, YN2, YP1, YP2) of column C1L. Since column C1L remains elastic during all cyclic tests, the average moments about x and y axes of the section, where the strain gauges are attached, can be defined by

$$M_{\mathrm{x}} = \epsilon_1 E S_{\mathrm{x}}, \quad M_{\mathrm{y}} = \epsilon_2 E S_{\mathrm{y}}, \tag{4}$$

where S_{x} and S_{y} are the elastic sectional moduli about the axes parallel to x and y axes of C1L section, respectively; and

$$\begin{aligned} \epsilon_1 &= \frac{1}{4}(\epsilon_{\mathrm{z5}} + \epsilon_{\mathrm{z6}} - \epsilon_{\mathrm{z7}} - \epsilon_{\mathrm{z8}}), \\ \epsilon_2 &= \frac{1}{4}(\epsilon_{\mathrm{z1}} + \epsilon_{\mathrm{z2}} - \epsilon_{\mathrm{z3}} - \epsilon_{\mathrm{z4}}). \end{aligned} \tag{5}$$

Similarly, M_{x} and M_{y} can be calculated for the section of column C1U. Note that M_{x} (or M_{y}) values for columns C1U and C1L have the same absolute value with opposite sign.

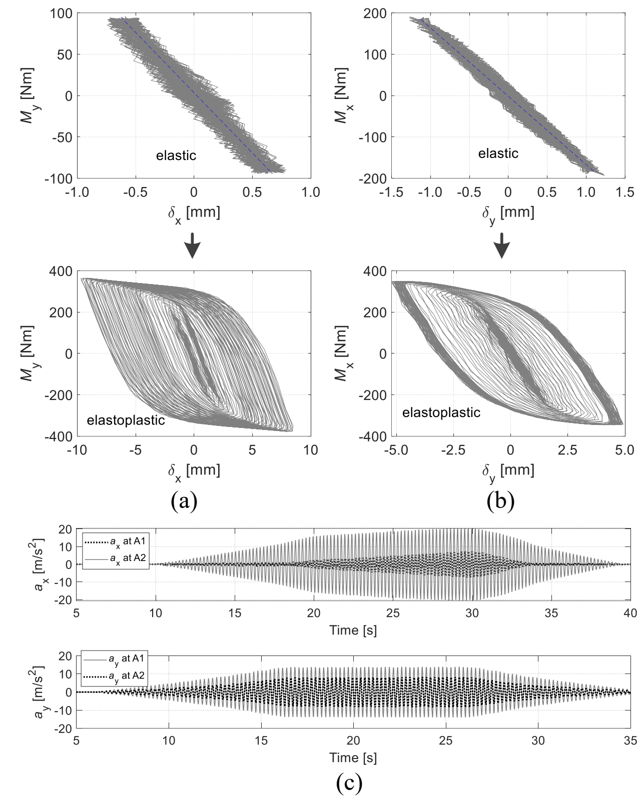

Figure 8: Examples of $M_\mathrm{y} - \delta_\mathrm{x}$ and $M_\mathrm{x} - \delta_\mathrm{y}$ curves in elastic and elastoplastic states of the structure, and acceleration histories at A1 and A2 on the floor. (a) $M_\mathrm{y} - \delta_\mathrm{x}$ curves; (b) $M_\mathrm{x} - \delta_\mathrm{y}$ curves; (c) a_x and a_y histories at A1 and A2.

Thus, column C1U, the specimen, and column C1L behave symmetrically with respect to the specimen like a column of a moment-resisting frame subjected to a lateral load.

Figures 8(a) and (b), respectively, show $M_\mathrm{y} - \delta_\mathrm{x}$ and $M_\mathrm{x} - \delta_\mathrm{y}$ curves obtained from the experimental results of four different cyclic tests. The upper and lower figures of Fig. 8(a) show two $M_\mathrm{y} - \delta_\mathrm{x}$ curves corresponding to the elastic and elastoplastic states of the specimen (or the structure), respectively, when the structure is subjected to two x-dir. waves with different magnitudes. Similar figures in Fig. 8(b) are for y-dir. waves. In the elastic state, the relationship between the moment and the relative displacement is measured, although it is not perfectly linear due to noise involved in the strain and displacement measurements. Meanwhile, the curves in the elastoplastic state confirm the hysteresis behavior of the specimen under severe cyclic loading. Thus, elastic and elastoplastic responses of interest are reliable indicators of cyclic elastic and elastoplastic properties of the specimen, respectively.

We are also interested in the accelerations at A1 and A2 on the floor because plastic deformations in the specimen are mainly triggered by the floor accelerations. The upper and lower figures of Fig. 8(c) show the histories of a_x and a_y, respectively, at both A1 and A2 measured from the cyclic tests associated with waves 4 and 8. As is clear, a_x at A2 is much larger than a_x at A1, and so with a_y at A1 and a_y at A2. Thus, a_x at A2 and a_y at A1 are considered as the accelerations of interest for the cyclic tests using waves 4 and 8, respectively.

By investigating the experimental results from all cyclic tests, we can classify the responses of interest into the following three groups according to the generated dynamic wave:

- x-dir. and (x-dir. and z-rot.) waves: a_x at A2, δ_x, and M_y.
- y-dir. and (y-dir. and z-rot) waves: a_y at A1, δ_y, and M_x.
- (x- and y-dirs.) wave: a_x at A2, a_y at A1, δ_x, M_y, and M_x.

Table 3: Ten cyclic tests used for parameter identification and verification.

No.	Wave ID	Specimen behavior	Responses of interest
1	1 (50%)	elastic	a_y at A1, δ_y, M_x
2	2 (120%)	elastoplastic	a_x at A2, a_y at A1, δ_x, M_y, M_x
3	3 (150%)	elastoplastic	a_x at A2, a_y at A1, δ_x, M_y, M_x
4	4 (140%)	elastoplastic	a_x at A2, δ_x, M_y
5	5 (120%)	elastoplastic	a_y at A1, δ_y, M_x
6	6 (80%)	elastic	a_x at A2, δ_x, M_y
7	6 (150%)	elastoplastic	a_x at A2, δ_x, M_y
8	7 (150%)	elastoplastic	a_x at A2, δ_x, M_y
9	8 (150%)	elastoplastic	a_y at A1, δ_y, M_x
10	9 (120%)	elastoplastic	a_x at A2, δ_x, M_y

4.2. Parameter identification problem

The experimental results of ten cyclic tests are selected for both identifying the material parameters and verifying the prediction performance of the resulting parameters. The selected tests, the status of the specimen, and the associated responses of interest are given in Table 3, where the number inside the brackets of wave ID is the scale factor for the corresponding wave amplitude in Table 2. Histories of the input accelerations at O calculated for the FE models associated with the selected tests are depicted in Fig. 9.

We divide the parameter identification process into two steps. The first step, as mentioned in Section 3, identifies Young's modulus values E, E_1, E_2, and E_3 from the cyclic elastic responses of the structure. This step is to validate the FE model in the elastic state before it is used to carry out costly cyclic elastoplastic simulations. The second step identifies the plastic parameters $\sigma_{\mathrm{y},0}$, Q_∞, b, C_1, and γ_1 from the cyclic elastoplastic responses of the structure. Thus, the first step uses the experimental results from tests No. 1 (y-dir. wave) and No. 6 (x-dir. wave) listed in Table 3 where the structure is within the elastic state, while the second step uses the experimental results from the remaining eight cyclic tests.

Let $f_i(\mathbf{x}_i)$: $\mathbb{R}^{n_i} \to \mathbb{R}$ denote the error function associated with the ith identification step ($i = 1, 2$). $f_i(\mathbf{x}_i)$ represents the difference between the measured histories of the responses of interest and the corresponding histories simulated from the FE model in Fig. 5, which is characterized by $\mathbf{x}_i$ and a specified set of input accelerations in Fig. 9. Here $n_1 = 4$ and $n_2 = 5$ because there are four and five material parameters to be identified in the first and second identification steps, respectively. By further assuming that modeling errors and observational noise are beyond the scope of this study and uncertainty in the parameters is neglected, the optimal $\mathbf{x}_i$ in the ith identification step can be found by solving

$$\begin{aligned} \underset{\mathbf{x}_i}{\text{minimize}} \quad & f_i(\mathbf{x}_i) \\ \text{subject to} \quad & \mathbf{x}_i \in [\mathbf{x}_{i\mathrm{l}}, \mathbf{x}_{i\mathrm{u}}] \quad (i = 1, 2), \end{aligned} \tag{6}$$

where $\mathbf{x}_1 = [E, E_1, E_2, E_3]$; $\mathbf{x}_2 = [\sigma_{\mathrm{y},0}, Q_\infty, b, C_1, \gamma_1]$; and $\mathbf{x}_{i\mathrm{l}}$ and $\mathbf{x}_{i\mathrm{u}}$ the specified lower and upper bounds of $\mathbf{x}_i$, respectively.

The error function $f_i(\mathbf{x}_i)$ can be formulated based on one of the responses of interest defined in Section 4.1. Nevertheless, as the floor accelerations intrinsically trigger

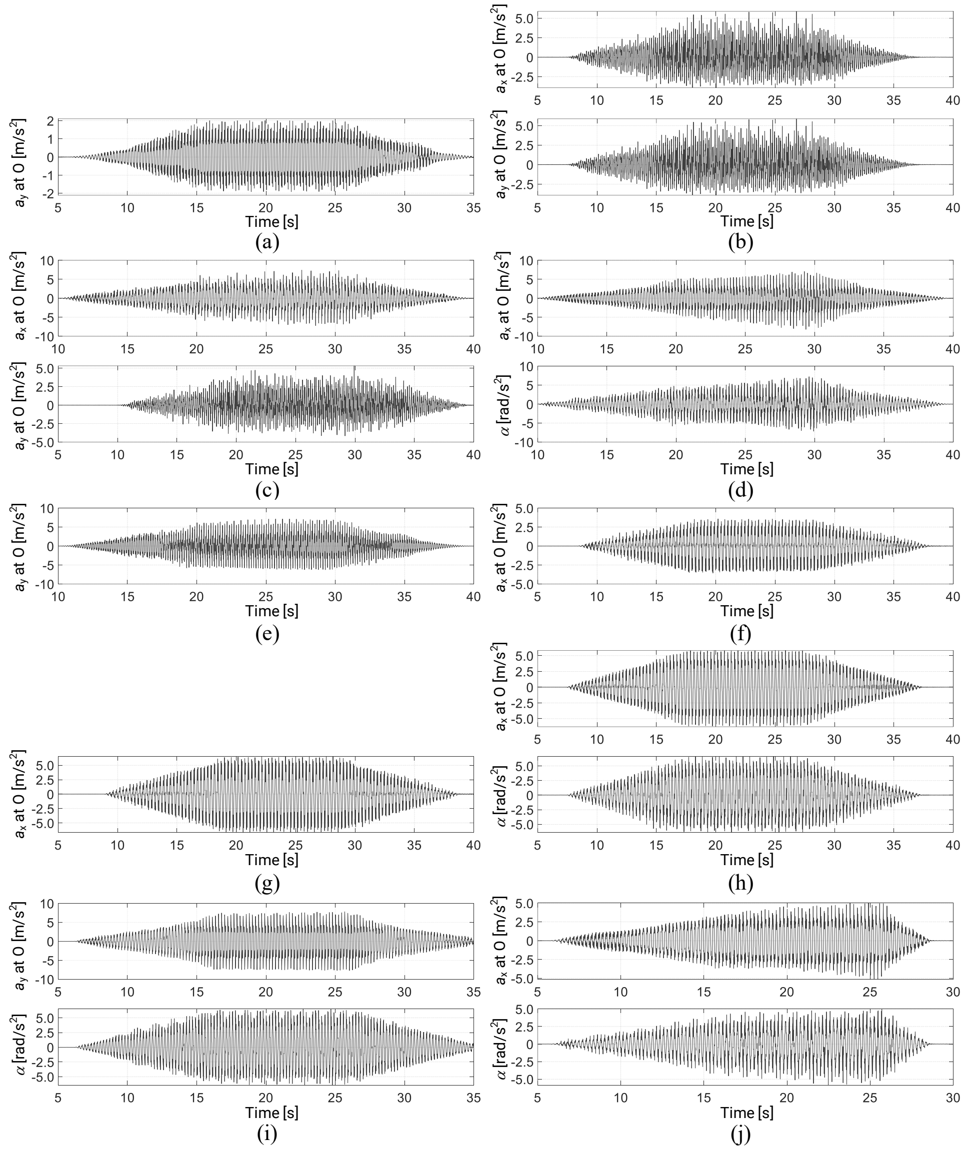

Figure 9: Input acceleration histories for the FE models associated with ten cyclic tests used for parameter identification and verification. (a)−(j) Nos. 1−10, respectively.

plastic deformations in the specimen, they are used to formulate $f_i(\mathbf{x}_i)$, and the relative displacements and bending moments are used to verify the prediction performance of identified parameters. Moreover, since it is computationally affordable to perform two cyclic elastic simulations for the structure, the accelerations of interest from tests Nos. 1

and 6 are simultaneously used for formulation of the error function in the first identification step. This aims to reduce the bias toward the experimental results obtained from a single cyclic test that may lead the identified parameters to inaccurate prediction of material behavior under other loading histories [24]. The second identification step, however, only uses the acceleration of interest from a single cyclic test to formulate the associated error function because using multiple waves is hindered by an enormous computational cost to complete a cyclic elastoplastic simulation for the structure. In our case, a single elastoplastic simulation averagely takes 40 minutes using a PC with an Intel(R) Xeon(R) E5-2643V4 3.40 GHz CPU and 64 GB memory.

Let $a^{\mathrm{s}}_{1,t}$ and $a^{\mathrm{m}}_{1,t}$ denote the simulated and measured values of the floor acceleration of interest at the tth time step of an acceleration history consisting of N_1 discrete steps measured from test No. 1. Similarly, $a^{\mathrm{s}}_{6,t}$ and $a^{\mathrm{m}}_{6,t}$ are defined for test No. 6 with an acceleration history of N_6 discrete steps. Following the root-mean-square deviation [9], the error function $f_1(\mathbf{x}_1)$ reads

$$f_1(\mathbf{x}_1) = \sqrt{\frac{1}{N_1}\sum_{t=1}^{N_1}\left(a^{\mathrm{s}}_{1,t}(\mathbf{x}_1) - a^{\mathrm{m}}_{1,t}\right)^2} + \sqrt{\frac{1}{N_6}\sum_{t=1}^{N_6}\left(a^{\mathrm{s}}_{6,t}(\mathbf{x}_1) - a^{\mathrm{m}}_{6,t}\right)^2}. \tag{7}$$

In the same manner, $f_2(\mathbf{x}_2)$ can be formulated as

$$f_2(\mathbf{x}_2) = \sqrt{\frac{1}{N_k}\sum_{t=1}^{N_k}\left(a^{\mathrm{s}}_{k,t}(\mathbf{x}_2) - a^{\mathrm{m}}_{k,t}\right)^2}, \tag{8}$$

where $a^{\mathrm{s}}_{k,t}$ and $a^{\mathrm{m}}_{k,t}$ are similarly defined as $a^{\mathrm{s}}_{1,t}$ and $a^{\mathrm{m}}_{1,t}$, respectively. However, they are associated with an acceleration history of N_k discrete steps measured from the kth test among eight cyclic tests that are used in the second identification step. If the responses of interest of the kth test include both a_{x} at A2 and a_{y} at A1, for example, for tests Nos. 2 and 3, a_{x} at A2 is selected for formulating f_2.

4.3. Solving the identification problem using Bayesian optimization

It may be infeasible to solve problem (6) using a gradient-based optimization algorithm because it is too costly to numerically evaluate the gradient of the error function $f_1(\mathbf{x}_1)$ and especially $f_2(\mathbf{x}_2)$. Although it is possible to use a population-based optimization algorithm, a large number of simulations required for obtaining a good solution makes its application restricted. BO [35–37], therefore, becomes an ideal candidate for solving the problem as it can provide a global-optimization framework for identification while keeping the number of costly simulations as small as possible. Our recent work [24] showed that BO outperforms some population-based algorithms in terms of the optimized error function value as well as the prediction performance of responses using identified parameters when expending the same number of simulation calls. In the following, we briefly describe the BO approach to handling problems (6), which is the same as the approach used in Ref. [24] with noise-free observations. To further simplify the exposition, we drop the subscripts of $f_1(\mathbf{x}_1)$ and $f_2(\mathbf{x}_2)$ hereafter because we equally treat the error functions and parameters in the two identification steps.

BO first creates a training dataset $\mathcal{D} = \{\mathbf{x}^n, f^n\}_{n=1}^N$, where $\mathbf{x}^n$ is a set of the parameters in the identification step of consideration and f^n the error function value associated with $\mathbf{x}^n$. The number of samples N is problem-dependent [24], and is assigned as $5n_1$ (i.e., 20) and $5n_2$ (i.e., 25) for the first and second identification steps, respectively. The samples $\mathbf{x}^n$ are randomly generated using Latin-hypercube sampling [39]. With $\mathbf{x}^n$ and the specified input acceleration histories, FE analyses of the experiment are carried out to evaluate $a^{\mathrm{s}}_{1,t}$ and $a^{\mathrm{s}}_{6,t}$ in Eq. (7) or $a^{\mathrm{s}}_{k,t}$ in Eq. (8), and f^n can be found accordingly. Once $\mathcal{D}$ has been created, we can sort the best parameter vector that provides the smallest error function value among those of $\mathcal{D}$, and let $f_{\min} = \min\{f^1, \ldots, f^N\}$.

Subsequently, BO constructs from $\mathcal{D}$ a Gaussian process (GP) model to probabilistically approximate the error function f, which is either f_1 in Eq. (7) or f_2 in Eq. (8). This GP model describes the relationship between f and $\mathbf{x}$ by a conditional Gaussian, denoted as $\hat{f}(\mathbf{x})$. The construction of $\hat{f}(\mathbf{x})$ is detailed in Appendix B. Following Eq. (B.6), the GP prediction of the error function value at a particular $\mathbf{x}$ reads

$$\hat{f}(\mathbf{x}) \sim \mathcal{N}\left(\mu_{\mathrm{f}}(\mathbf{x}), \tau_{\mathrm{f}}^2(\mathbf{x})\right), \tag{9}$$

where $\mathcal{N}$ denotes a univariate Gaussian; and $\mu_{\mathrm{f}}(\mathbf{x})$ and $\tau_{\mathrm{f}}(\mathbf{x})$ the mean and standard deviation of $\hat{f}(\mathbf{x})$, respectively.

Now suppose BO has completed its sth iteration and has to specify a new sampling point $\mathbf{x}^{s+1}$ at which the FE analysis is carried out to evaluate $f(\mathbf{x}^{s+1})$ in the next step, i.e., $(s+1)$th step, that, in turn, updates the current training dataset, the best-observed parameter vector, and the current GP model. Since we aim to reduce the number of costly simulations as much as possible, $\mathbf{x}^{s+1}$ should be ideal in the parameter space, and finding it should not require any costly simulation. For this purpose, BO allows us to transform how promising each point in the parameter space is into a measure of our belief about an improvement in the best-observed parameter vector using an acquisition function formulated based on the current GP model. Thus, the new sampling point $\mathbf{x}^{s+1}$ is the maximizer of such an acquisition function. By further adopting the well-known expected improvement (EI) acquisition function proposed by Jones et al. [35], $\mathbf{x}^{s+1}$ can be found by solving [24]

$$\begin{aligned} \text{find} \quad & \mathbf{x}^{s+1} = \underset{\mathbf{x}}{\operatorname{argmax}} \quad EI(\mathbf{x}) \\ \text{subject to} \quad & \mathbf{x} \in [\mathbf{x}_{\mathrm{l}}, \mathbf{x}_{\mathrm{u}}], \end{aligned} \tag{10}$$

where $\mathbf{x}_{\mathrm{l}}$ and $\mathbf{x}_{\mathrm{u}}$ represent $\mathbf{x}_{il}$ and $\mathbf{x}_{i\mathrm{u}}$, respectively; and

$$EI(\mathbf{x}) = (f_{\min} - \mu_{\mathrm{f}}(\mathbf{x}))\, \Phi\left(\frac{f_{\min} - \mu_{\mathrm{f}}(\mathbf{x})}{\tau_{\mathrm{f}}(\mathbf{x})}\right) + \tau_{\mathrm{f}}(\mathbf{x})\phi\left(\frac{f_{\min} - \mu_{\mathrm{f}}(\mathbf{x})}{\tau_{\mathrm{f}}(\mathbf{x})}\right), \tag{11}$$

where $\mu_{\mathrm{f}}(\mathbf{x})$ and $\tau_{\mathrm{f}}(\mathbf{x})$ are defined in Eq. (9); and $\Phi(\cdot)$ and $\phi(\cdot)$ the standard normal cumulative distribution and probability density functions, respectively. Because EI is formulated from $f_{\min}$ and the current GP model, finding $\mathbf{x}^{s+1}$ does not require any additional costly simulation. The power of this acquisition function arises from its ability to perfectly balance exploitation (the first term) and exploration (the second term) in the parameter space. Another advantage in use of EI is that maximizing it does not reselect the members of $\mathcal{D}$ because it always takes non-positive values at these members.

In summary, the following five substeps are sequentially performed in each identification step:

- Substep 1: Generate initial samples of parameters $\mathbf{x}$ using Latin-hypercube sampling. Then, create the training dataset $\mathcal{D}$ by performing FE analyses for the generated samples.
- Substep 2: Find the best parameter vector among the samples of $\mathcal{D}$ that is associated with $f_{\min}$. Terminate the identification and output the parameters if the number of BO iterations reaches a specified upper limit. Otherwise, proceed to Substep 3.
- Substep 3: Construct GP model for $f(\mathbf{x})$ based on $\mathcal{D}$; see Appendix B.

- Substep 4: Find $\mathbf{x}^{s+1}$ by solving problem (10).
- Substep 5: Evaluate $f(\mathbf{x}^{s+1})$ using the FE analysis, update $\mathcal{D}$ by adding $\mathbf{x}^{s+1}$ and $f(\mathbf{x}^{s+1})$, and go to Substep 2.

5. Identification and verification results

5.1. Initial settings

Table 4 provides the intervals for nine material parameters to be identified in the two identification steps. Small intervals assigned for E and $\sigma_{\mathrm{y},0}$ are derived from the experimental results of the monotonic tension tests in Section 2.2. The intervals for E_1, E_2, and E_3 cover the common Young's modulus values for structural steels. Those for Q_∞, b, C_1, and γ_1 are taken from Ref. [24].

Table 4: Material parameter intervals.

Parameter	Lower bound	Upper bound
E [GPa]	200	210
E_1, E_2, E_3 [GPa]	185	215
$\sigma_{\mathrm{y},0}$ [MPa]	270	290
Q_∞ [MPa]	10	100
b	5	25
C_1 [MPa]	2000	10000
γ_1	10	100

BO is performed three times in the first identification step, thereby producing three sets of Young's modulus values. Each of these sets is then used as input to the FE model for finding the plastic parameters in the second identification step. The second identification step, in turn, selects five among eight elastoplastic cyclic tests in Table 3 for finding the plastic parameters. The selected tests include No. 2 (x- and y-dir. wave), No. 5 (y-dir. wave), No. 7 (x-dir. wave), No. 8 (x-dir. and z-rot. wave), and No. 9 (y-dir. and z-rot. wave), which are further indexed as identification cases 1, 2, 3, 4, and 5, respectively. Thus, each identification case, together with the three Young's modulus sets found in the first identification step, offers three sets of material parameters, and the best set of identified parameters corresponds to the smallest value of f_2. The remaining three elastoplastic cyclic tests, namely, No. 3 (x- and y-dir. wave), No. 4 (x-dir. and z-rot. wave), and No. 10 (x-dir. and z-rot. wave) are used as verification tests to assess the prediction performance of the best set of identified parameters from each identification case.

Problem (10) is solved in each BO iteration using genetic algorithm (GA). Parameters for GA including the population size, maximum number of generations, crossover fraction, number of elite transfer, and tolerance for the objective and constraint functions are 2000, 50, 65%, 2, and 10^{-6}, respectively. Here, GA uses a large population size to increase the chance of finding the global maximizer of EI in each BO iteration predicted by the current GP model, which can reduce the effect of its randomness on the BO performance. The numbers of BO iterations for the first and second identification steps are limited at 25 and 30, respectively. Thus, the respective numbers of simulation calls are 90 (i.e., $20 \times 2 = 40$ for training the initial GP model and $25 \times 2 = 50$ for BO iterations) and 55 (i.e., 25 for training the initial GP model and 30 for BO iterations).

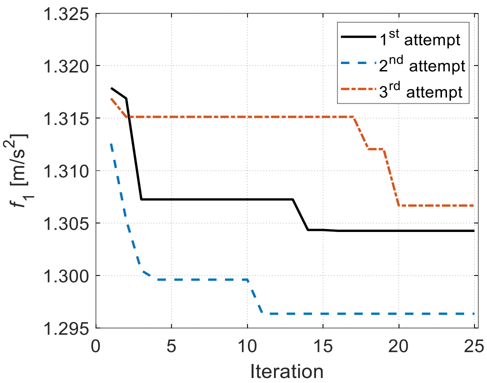

Figure 10: Histories of three BO attempts of the first identification step.

5.2. *Young's modulus values from the first identification step*

Figure 10 shows the histories of three BO attempts for three different training datasets generated in the first identification step. The value of f_1 from each BO is not considerably improved since the very first iterations of the algorithm, and there is no major difference in the final values of f_1 obtained from the three BO attempts. This may be explained by the fact that the best set of Young's modulus values found in the first iteration of each BO attempt can accurately predict the accelerations measured from tests Nos. 1 and 6 as the allowable ranges of Young's modulus are very small. Table 5 compares three sets of Young's modulus values obtained from the three BO attempts. Three sets of E, E_2, and E_3 are quite similar. A considerable difference in three E_1 values indicates that it is less important to the sensitivity of f_1 than E, E_2, and E_3.

Table 5: Comparison of three sets of Young's modulus values obtained from three BO attempts of the first identification step.

Parameter	1st attempt	2nd attempt	3rd attempt
E [GPa]	206.35	210.00	205.34
E_1 [GPa]	202.42	212.90	196.77
E_2 [GPa]	209.24	211.23	207.43
E_3 [GPa]	215.00	215.00	215.00
f_1 [m/s^2]	1.304	1.296	1.307

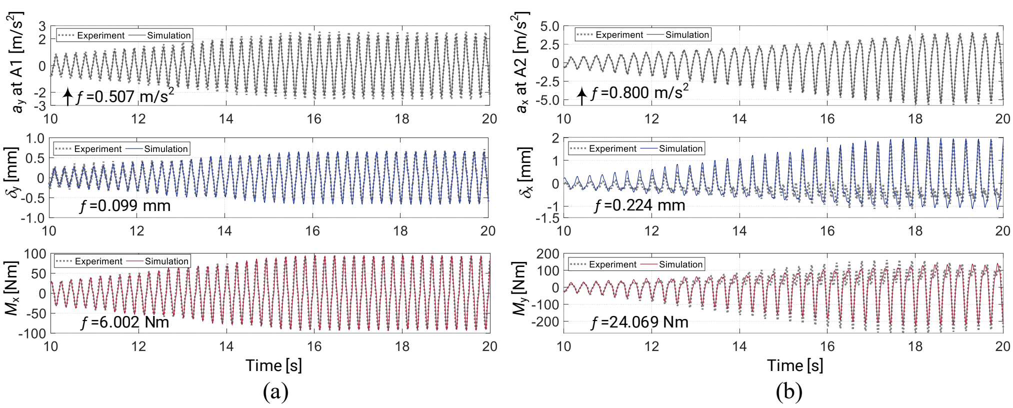

Figure 11: Comparison of test data and simulated values of the responses of interest from tests Nos. 1 and 6 with use of Young's modulus values identified from the 3rd BO attempt for the predictions. Arrows indicate the responses used for formulating f_1. (a) Test No. 1; (b) Test No. 6.

Figure 11 compares the histories of the responses of interest measured from tests Nos. 1 and 6, and the corresponding histories simulated using the set of Young's modulus values obtained from the 3rd BO attempt, where the arrow at the lower-left corner of the figure indicates the acceleration history used for formulating f_1, and the error value f is evaluated using Eq. (7) for the response in the figure. Although the 3rd BO attempt provides the worst optimal value of f_1 among the three values obtained in this step, there is a good agreement between the measured and simulated histories of the responses of interest from tests Nos. 1 and 6. This result also validates the FE model when it is used for simulating the cyclic behavior of the structure in the elastic state.

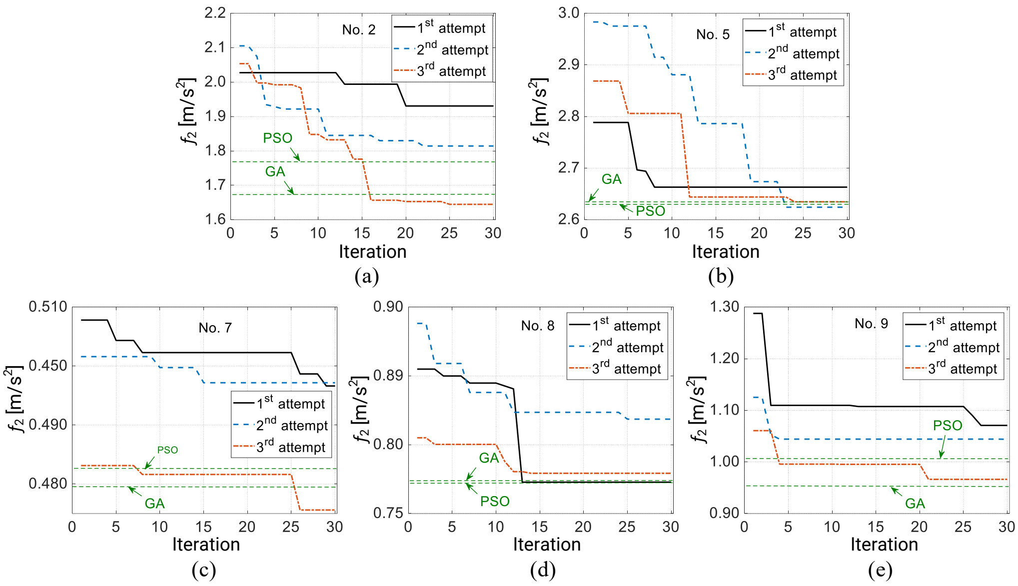

Figure 12: Histories of three BO attempts of each identification case in the second identification step and the comparison of the minimum values of f_2 obtained from the 3rd BO attempt, GA, and PSO. (a)−(e) Cases 1−5, respectively.

5.3. Plastic parameters from the second identification step and verification

Figure 12 shows the histories of three BO attempts of each identification case in the second identification step. In all identification cases, BO considerably reduces the error function as it terminates. It is also natural to obtain three different optimized values of f_2 in each identification case because the 1st, 2nd, and 3rd BO attempts of each case use the 1st, 2nd, and 3rd sets of Young's modulus values found in the first identification step, respectively. The 3rd BO attempt of identification cases 1, 3, and 5 offers the best

Table 6: Comparison of the best parameter sets obtained from five identification cases in the second identification step.

Parameter	Case 1	Case 2	Case 3	Case 4	Case 5
E [GPa]	205.34	210.00	205.34	206.35	205.34
E_1 [GPa]	196.77	212.90	196.77	202.42	196.77
E_2 [GPa]	207.43	211.23	207.43	209.24	207.43
E_3 [GPa]	215.00	215.00	215.00	215.00	215.00
$\sigma_{\mathrm{y},0}$ [MPa]	270.00	271.37	272.58	270.12	277.77
Q_∞ [MPa]	10.00	12.75	10.20	10.37	10.03
b	22.51	7.32	11.50	5.00	5.01
C_1 [MPa]	2000.00	3666.18	7594.39	2000.62	9984.83
γ_1	39.96	10.01	13.64	91.85	11.81
f_2 [m/s^2]	1.645	2.624	0.476	0.773	0.966

optimal value of f_2 among the three attempts even though it corresponds to the worst set of Young's modulus values. The 3rd BO attempt of identification cases 2 and 4 also provides good values of f_2.

For comparison purpose, we use GA and particle swarm optimization (PSO) algorithm, each characterized by five generations and a population of size 12, to directly solve problem (6) formulated for each identification case with the 3rd set of Young's modulus values obtained from the first identification step. Thus, the number of simulation calls required for either GA or PSO is 60, which is greater than 55 for the BO attempt of each identification case. The minimum values of f_2 obtained from GA and PSO provide baselines for comparison with f_2 obtained from the 3rd BO attempt of each identification case. Comparison results in Fig. 12 show that the minimum values of f_2 obtained from GA as well as PSO are not significantly better or even worse than f_2 obtained from the 3rd BO attempt of each identification case, let alone that BO quickly reaches the minimum value of f_2 before it terminates. This indicates the robustness of BO to solve the identification problem.

Table 6 lists the best parameter set identified from each identification case. $\sigma_{\mathrm{y},0}$ values obtained from cases 1, 2, 3, and 4 are similar, and are slightly smaller than the value obtained from case 5. Q_∞ from all cases tends to concentrate to its lower bound, indicating that the stress saturation of the specimen is not far from $\sigma_{\mathrm{y},0}$. The identified values of b, C_1, and γ_1 are case-dependent.

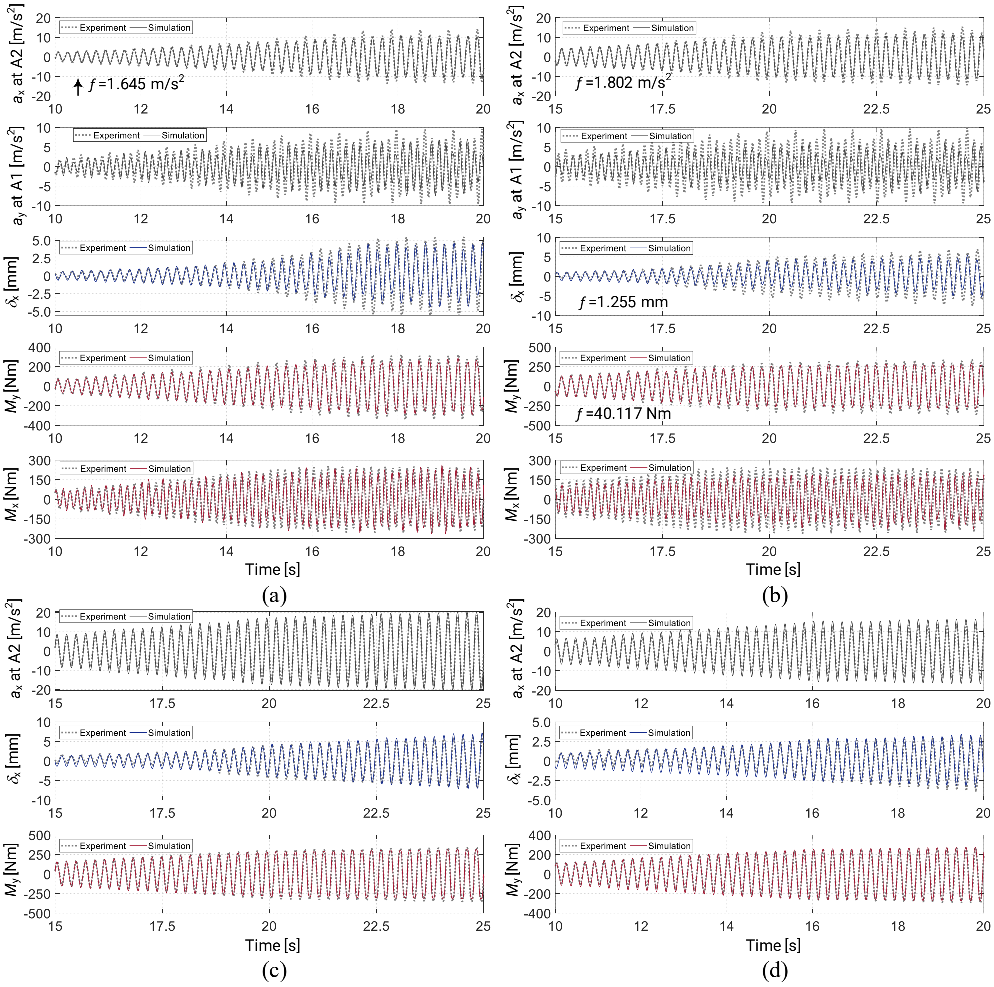

Figure 13: Comparison of test data and simulated values of the responses of interest from the test used for identification and from the verification tests using the best parameter set found from case 1 (i.e., No. 2) for the predictions. Arrow indicates the response used for formulating f_2. (a) Test No. 2; (b) Test No. 3; (b) Test No. 4; (d) Test No. 10.

Figures 13, 14, 15, 16, and 17 compare the measured and simulated responses of interest from the three verification tests (i.e., Nos. 3, 4, and 10) using the best parameter sets identified from cases 1, 2, 3, 4, and 5 for predictions, respectively. The comparison between the measured and simulated responses of interest from the test used in each identification case is also given. The arrow in each figure indicates the acceleration history used in the identification case to formulate f_2. It is confirmed that the best parameter set found in each identification case can reproduce the histories of the responses of interest measured from the verification tests that are not used for identification. They can also predict the responses that are not used for formulating f_2 in each identification case with acceptable accuracy.

Table 7: Comparison of prediction performances of the best parameter sets obtained from five identification cases on three responses of interest of test No. 3 (x- and y-dir. wave).

Identification case	f for a_{x} at A2 [m/s^2]	f for δ_{x} [mm]	f for M_{y} [Nm]
Case 1 (x- and y-dir.)	1.802	1.255	40.117
Case 2 (y-dir.)	2.074	1.722	47.419
Case 3 (x-dir.)	2.414	1.693	53.075
Case 4 (x-dir. and z-rot.)	2.192	1.637	46.995
Case 5 (y-dir. and z-rot.)	2.035	1.667	41.683

To quantitatively compare the prediction performances of the best parameter sets obtained from the five identification cases, we use Eq. (8) to evaluate the error (i.e., f_2) values for the measured and simulated responses of a_{x} at A2, δ_{x}, and M_{y} from verification test No. 3 (x- and y-dir. wave). The resulting error values associated with each identification case are shown in Figs. 13(b), 14(b), 15(b), 16(b), and 17(b), and also listed in Table 7. Comparison results show that the prediction performance of the best parameter set in case 1 (x- and y-dir. wave) is much better than that in cases 2 (y-dir. wave) and 3 (x-dir. wave). The prediction performance of the best parameter set in case 4 (x-dir. and z-rot. wave) is better than that in case 3 (x-dir. wave), and so with case 5 (y-dir. and z-rot. wave) and case 2 (y-dir. wave). These results indicate that the best set of material parameters identified from the structural response associated with a multi-directional wave has a better prediction performance than that associated with a single-directional wave. Moreover, there exists the dataset-specific bias as the parameter

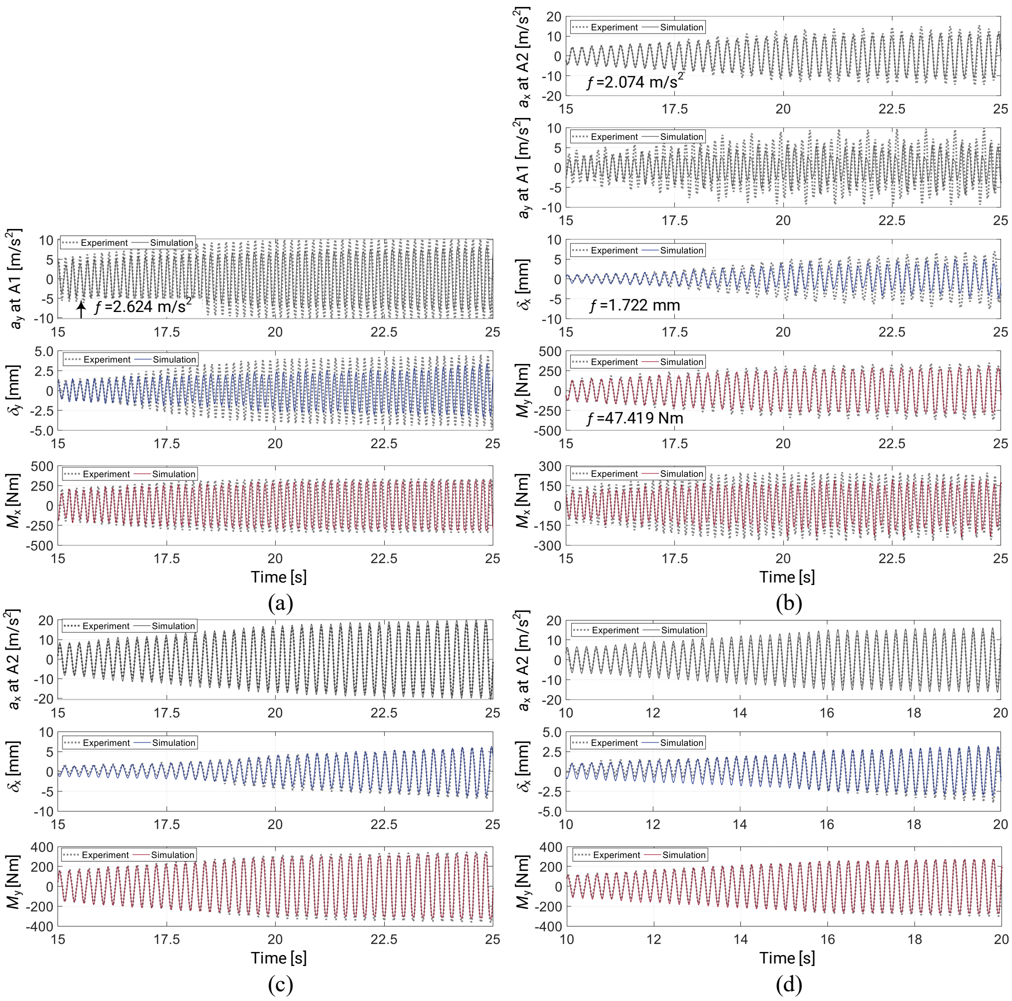

Figure 14: Comparison of test data and simulated values of the responses of interest from the test used for identification and from the verification tests using the best parameter set found from case 2 (i.e., No. 5) for the predictions. Arrow indicates the response used for formulating f_2. (a) Test No. 5; (b) Test No. 3; (b) Test No. 4; (d) Test No. 10.

set identified from case 1 (x- and y-dir. wave) provides extremely good predictions of the responses measured from test No. 3, which also uses x- and y-dir. wave. Note that it is also desirable to simulate the cyclic uni-axial behavior of the specimen using the parameters identified from the multi-axial cyclic loading tests. However, cyclic material tests are not available for the specimen.

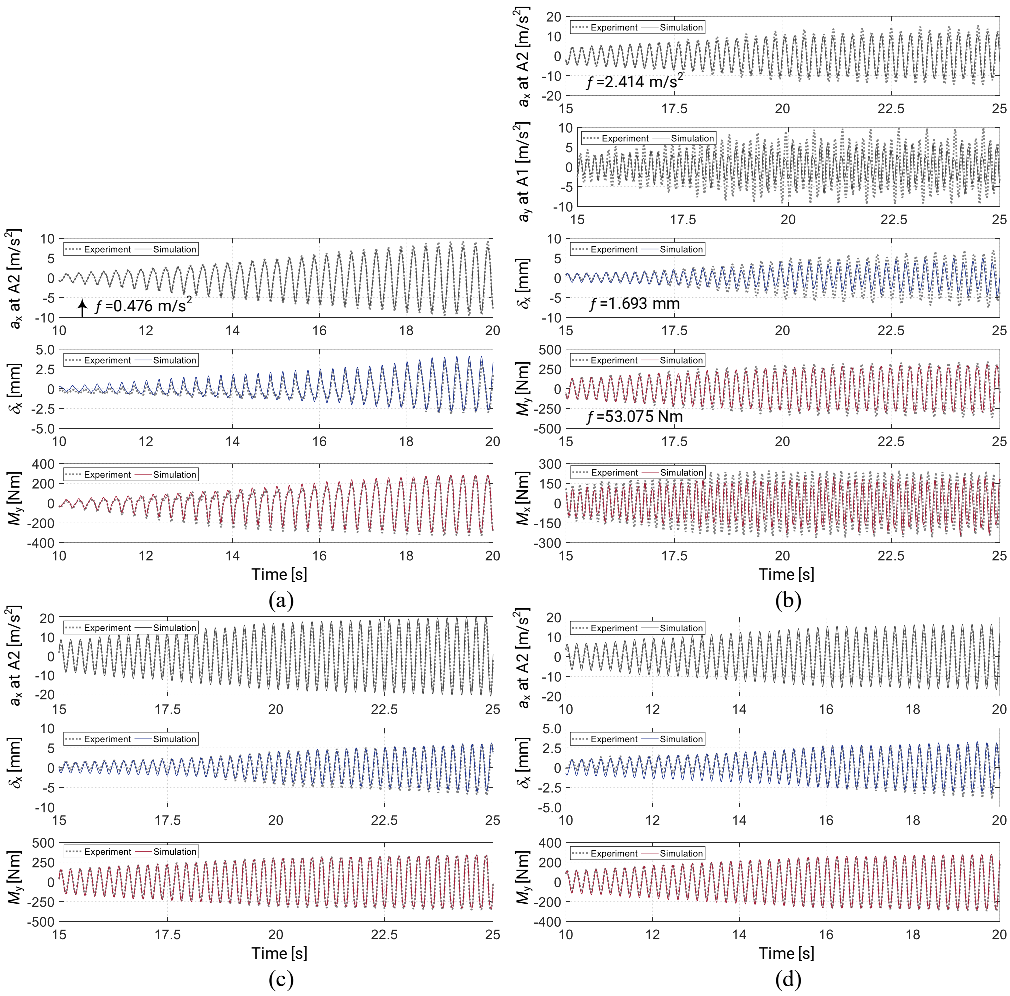

Figure 15: Comparison of test data and simulated values of the responses of interest from the test used for identification and from the verification tests using the best parameter set found from case 3 (i.e., No. 7). Arrow indicates the response used for formulating f_2. (a) Test No. 7; (b) Test No. 3; (b) Test No. 4; (d) Test No. 10.

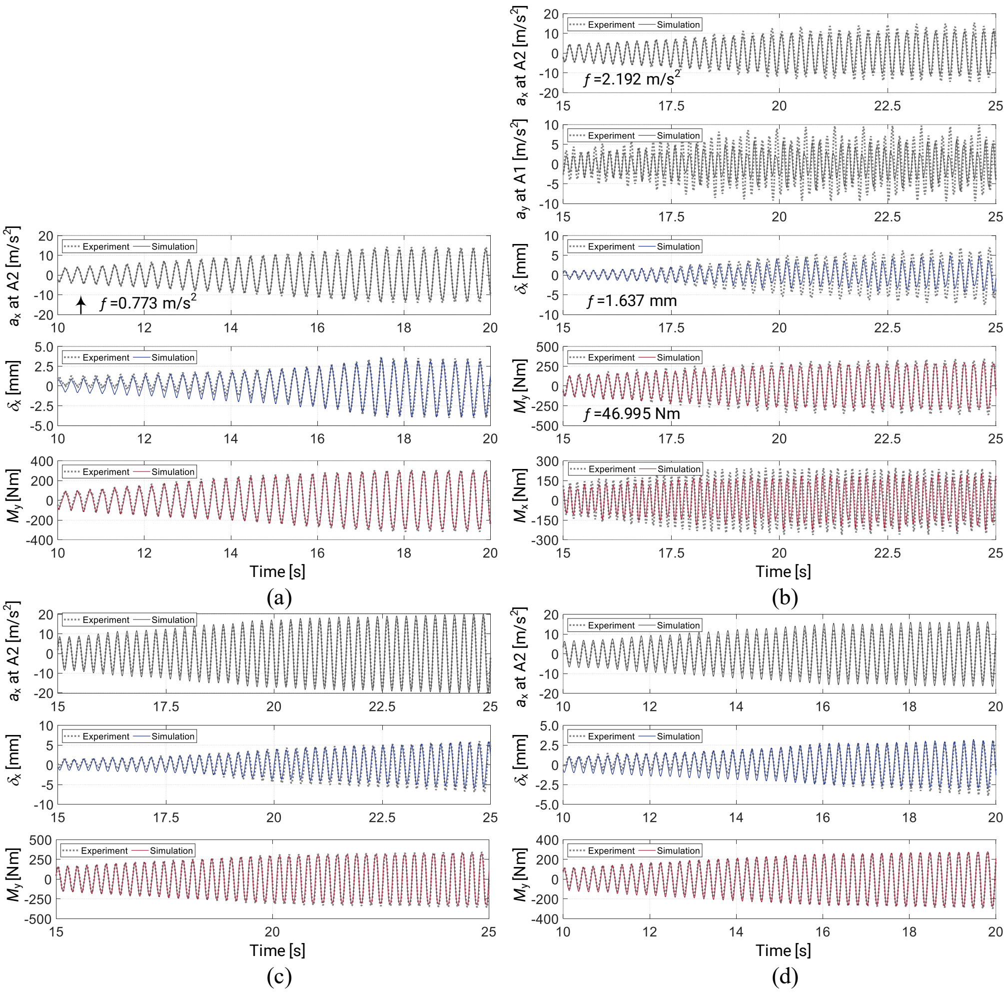

Figure 16: Comparison of test data and simulated values of the responses of interest from the test used for identification and from the verification tests using the best parameter set found from case 4 (i.e., No. 8). Arrow indicates the response used for formulating f_2. (a) Test No. 8; (b) Test No. 3; (b) Test No. 4; (d) Test No. 10.

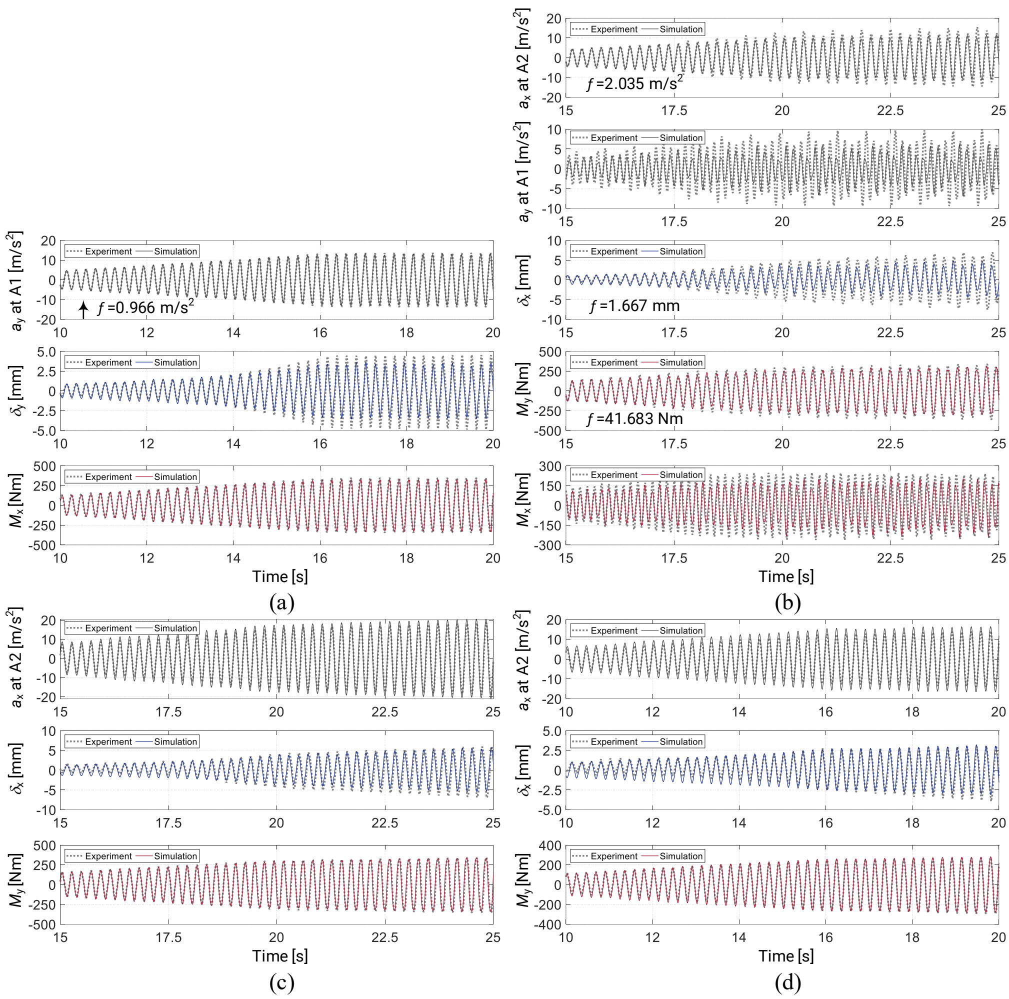

Figure 17: Comparison of test data and simulated values of the responses of interest from the test used for identification and from the verification tests using the best parameter set found from case 5 (i.e., No. 9). Arrow indicates the response used for formulating f_2. (a) Test No. 9; (b) Test No. 3; (b) Test No. 4; (d) Test No. 10.

6. Conclusions

We have proposed a two-step BO approach to inverse identification of the cyclic constitutive law for a steel specimen of a structure subjected to multi-axial cyclic loading. A series of cyclic tests is conducted on the structure where the specimen is the only member experiencing the hardening process when the structure is subjected to cyclic loading. The cyclic responses of the structure at the locations of interest are measured, and then used for formulating an inverse problem to identify the material parameters for an FE model that incorporates the linear elastic and nonlinear combined isotropic/kinematic hardening models to simulate the cyclic behaviors of the structure in both the elastic and elastoplastic states. Subsequently, the formulated inverse problem is solved using BO to keep the number of costly simulations as small as possible. Finally, the prediction performance of the identified material parameters is verified against the experimental results from different cyclic tests with various cyclic loading conditions. The main conclusions are summarized as follows:

- With the presented experimental program, the multi-axial cyclic elastoplastic behavior of a steel specimen can be investigated through the acceleration responses of a structure. This is remarkable because it is more difficult to carry out a cyclic material test than to perform a cyclic structural test.
- The proposed two-step BO approach has successfully identified the material parameters for modeling the material behavior of the structure using its responses while limiting the number of costly simulations. The identified parameters can accurately predict the cyclic responses of the structure under different cyclic loading conditions, and in both elastic and plastic states.
- Verification results indicate that the material parameters identified from the structural response associated with a multi-directional wave may have a better prediction performance than those associated with a single-directional wave.
- The error function obtained from BO approaches outperforms those from GA and PSO, even though BO expends less number of costly simulations than GA and PSO. This indicates the effectiveness of BO to solve the formulated identification problem.

- Results in Table 7 show that there exists the dataset-specific bias leading the parameters identified from the response associated with a loading condition to provide very good predictions of responses associated with a similar loading condition. In other words, the resulting parameters may lead to an overfitted numerical model. Do and Ohsaki [24] showed that such a model may give inaccurate predictions of material behavior under other loading conditions and suggested utilizing several datasets for identification. This requires further research on overfitting, its effects on structural response predictions, and how to avoid it in parameter identification.

Acknowledgments

This work is supported by the JICA AUN/SEED-Net project and by JSPS KAKENHI under Grant Number JP19H02286. Valuable comments from Prof. Miyamura (Nihon University) and Dr. Yamamoto (Takenaka Corporation) are acknowledged.

Research data

Data of input accelerations and measured responses of interest for ten cyclic tests in Table 3 are available online at `https://doi.org/10.5281/zenodo.7159424`.

Appendix A: Nonlinear combined isotropic/kinematic hardening model

The relationship between strain and stress states of structural steel is established from its current status that is either elastic or plastic, and can be detected using the following von Mises yield condition:

$$F = \|\boldsymbol{\xi}\| - \sqrt{\frac{2}{3}}\sigma_{\mathrm{y}} \leq 0, \tag{A.1}$$

where $\boldsymbol{\xi} = \mathrm{dev}[\boldsymbol{\sigma}] - \mathrm{dev}[\boldsymbol{\alpha}]$ the shifted-stress tensor; $\mathrm{dev}[\cdot]$ the deviatoric part of $[\cdot]$; $\|\cdot\|$ the 2-norm of the tensor; $\boldsymbol{\sigma}$ the stress tensor at a point of a steel body; $\boldsymbol{\alpha}$ the back-stress tensor; and σ_{y} the yield stress.

Isotropic and kinematic hardening models are often used for describing the strain hardening process of structural steels subjected to cyclic loading. The isotropic hardening model only increases the size of the yield surface $F = 0$ during the evolution of plastic deformations. Thus, $\boldsymbol{\alpha}$ does not appear in Eq. (A.1), leading the yield surface to be an isotropic function of the stress that cannot capture the Bauschinger effect [40]. As structural steels exhibit a saturation point of the stress at large deformation, the isotropic hardening model can describe the increment of the size of the yield surface using the following Voce hardening law [41]:

$$\sigma_{\mathrm{y}} = \sigma_{\mathrm{y},0} + Q_{\infty}[1 - \exp(-b\epsilon_{\mathrm{eq}}^{\mathrm{p}})], \tag{A.2}$$

where $\sigma_{\mathrm{y},0}$ denotes the initial yield stress; Q_{∞} the difference of the stress saturation and $\sigma_{\mathrm{y},0}$; b the isotropic saturation rate; and $\epsilon_{\mathrm{eq}}^{\mathrm{p}}$ the current equivalent plastic strain determined based on its previous state and the rate $\dot{\epsilon}_{\mathrm{eq}}^{\mathrm{p}}$.

The kinematic hardening model, on the other hand, does not change the size and shape of the yield surface. Instead, it updates the center of the yield surface using a rigid translation in the evolution direction of the plastic strain. This enables the kinematic hardening model to capture the Bauschinger effect. The back-stress tensor $\boldsymbol{\alpha}$ can be further decomposed into n_{k} back-stress components for a better approximation as [42]

$$\boldsymbol{\alpha} = \sum_{k=1}^{n_{\mathrm{k}}} \boldsymbol{\alpha}_k, \tag{A.3}$$

where the rate of $\boldsymbol{\alpha}_k$ can be described by a the following nonlinear kinematic hardening rule [43]:

$$\dot{\boldsymbol{\alpha}}_k = \sqrt{\frac{2}{3}} C_k \dot{\epsilon}_{\mathrm{eq}}^{\mathrm{p}} \mathbf{n} - \gamma_k \dot{\epsilon}_{\mathrm{eq}}^{\mathrm{p}} \boldsymbol{\alpha}_k, \tag{A.4}$$

where $\mathbf{n} = \boldsymbol{\xi}/\|\boldsymbol{\xi}\|$ the unit normal vector of the yield surface; and C_k and γ_k the translation and relaxation rates of $\boldsymbol{\alpha}_k$, respectively.

The nonlinear combined isotropic/kinematic hardening model was developed with Eqs. (A.2) and (A.4) for simultaneous use of the properties of isotropic and nonlinear kinematic hardening. Let $\mathbf{x} = [x_1, \ldots, x_n] \in \mathbb{R}^n$ denote the vector of n material parameters for such a hardening model. Thus, $\mathbf{x} = [E, Q_{\infty}, b, \sigma_{\mathrm{y},0}, C_1, \gamma_1]$ if we use one back-stress component in Eq. (A.3) and a fixed Poisson's ratio, where E is Young's modulus of the material.

Appendix B: Gaussian process modeling

Consider the training dataset $\mathcal{D} = \{\mathbf{x}^n, f^n\}_{n=1}^N$, where $\mathbf{x}^n$ are vectors of the material parameters and f^n the corresponding error function values. Based on $\mathcal{D}$, we wish to establish the mapping from $\mathbf{x}$ to f, i.e., $f = \hat{f}(\mathbf{x})$.

GP modeling assumes that any finite subset of an infinite set of the error function values has a joint Gaussian distribution [44]. Thus, for the set $\{\mathbf{x}^1, \ldots, \mathbf{x}^N\}$, the corresponding error function values $\{f^1, \ldots, f^N\}$ are distributed according to

$$\begin{bmatrix} f^1 \\ \vdots \\ f^N \end{bmatrix} \sim \mathcal{N}_N \left(\begin{bmatrix} m(\mathbf{x}^1) \\ \vdots \\ m(\mathbf{x}^N) \end{bmatrix}, \begin{bmatrix} k(\mathbf{x}^1, \mathbf{x}^1) & \cdots & k(\mathbf{x}^1, \mathbf{x}^N) \\ \vdots & \ddots & \vdots \\ k(\mathbf{x}^N, \mathbf{x}^1) & \cdots & k(\mathbf{x}^N, \mathbf{x}^N) \end{bmatrix} \right), \tag{B.1}$$

where $\mathcal{N}_N$ denotes an N-variate Gaussian; and $m(\mathbf{x}) = \mathbb{E}[\hat{f}(\mathbf{x})]$ and $k(\mathbf{x}, \mathbf{x}')$ the mean and covariance kernel functions, respectively. Here, the mean function is set as $m(\mathbf{x}) = 0$ because $k(\mathbf{x}, \mathbf{x}')$ is flexible enough to handle the role of $m(\mathbf{x})$ [44]. $k(\mathbf{x}, \mathbf{x}')$ is defined for any pair of the parameter vectors $\mathbf{x}$ and $\mathbf{x}'$ to measure the similarity between two corresponding error function values $f = \hat{f}(\mathbf{x})$ and $f = \hat{f}(\mathbf{x}')$, such that

$$k(\mathbf{x}, \mathbf{x}') = \mathbb{E}\big[\big(\hat{f}(\mathbf{x}) - m(\mathbf{x})\big)\big(\hat{f}(\mathbf{x}') - m(\mathbf{x}')\big)\big]. \tag{B.2}$$

We use the well-known squared exponential kernel as

$$k(\mathbf{x}, \mathbf{x}') = \exp\left(-\frac{(\mathbf{x} - \mathbf{x}')^T (\mathbf{x} - \mathbf{x}')}{2l^2} \right), \tag{B.3}$$

where l denotes the characteristic length-scale parameter that is determined by using the maximum likelihood estimation of $\mathcal{D}$ [44].

Once l has been determined, we wish to use the information in Eq. (B.1) for predicting the error function value f^* at a new parameter vector $\mathbf{x}^*$, i.e., $f^*|\mathbf{f} = \hat{f}(\mathbf{x}^*)$, where $\mathbf{f} = [f^1, \ldots, f^N]^T$. As the GP nature, the joint PDF of f^* and $\mathbf{f}$ is also a Gaussian as

$$\begin{bmatrix} f^* \\ \mathbf{f} \end{bmatrix} \sim \mathcal{N}_{N+1} \left(\begin{bmatrix} m(\mathbf{x}^*) \\ \mathbf{m}(\mathbf{X}) \end{bmatrix}, \begin{bmatrix} k(\mathbf{x}^*, \mathbf{x}^*) & \mathbf{K}(\mathbf{x}^*, \mathbf{X}) \\ \mathbf{K}(\mathbf{x}^*, \mathbf{X})^T & \mathbf{K}(\mathbf{X}, \mathbf{X}) \end{bmatrix} \right), \tag{B.4}$$

where $\mathbf{X} = [\mathbf{x}^1, \ldots, \mathbf{x}^N]^T$, $\mathbf{m}(\mathbf{X}) = [m(\mathbf{x}_1), \ldots, m(\mathbf{x}_N)]^T$, and

$$\begin{aligned} \mathbf{K}(\mathbf{x}^*, \mathbf{X}) &= \big[k(\mathbf{x}^*, \mathbf{x}^1), \ldots, k(\mathbf{x}^*, \mathbf{x}^N)\big], \\ \mathbf{K}(\mathbf{X}, \mathbf{X}) &= \begin{bmatrix} k(\mathbf{x}^1, \mathbf{x}^1) & \cdots & k(\mathbf{x}^1, \mathbf{x}^N) \\ \vdots & \ddots & \vdots \\ k(\mathbf{x}^N, \mathbf{x}^1) & \cdots & k(\mathbf{x}^N, \mathbf{x}^N) \end{bmatrix}. \end{aligned} \tag{B.5}$$

The conditional Gaussian variable $f^*|\mathbf{f} = \hat{f}(\mathbf{x}^*)$ can be derived from Eq. (B.4) using the standard conditioning rule [44], such that

$$f^*|\mathbf{f} \sim \mathcal{N}\left(\mu_{\mathrm{f}^*}(\mathbf{x}^*), \tau_{\mathrm{f}^*}^2(\mathbf{x}^*)\right), \tag{B.6}$$

where

$$\begin{aligned} \mu_{\mathrm{f}^*}(\mathbf{x}^*) &= m(\mathbf{x}^*) + \mathbf{K}(\mathbf{x}^*, \mathbf{X})\mathbf{K}(\mathbf{X}, \mathbf{X})^{-1}\left(\mathbf{f} - \mathbf{m}(\mathbf{X})\right), \\ \tau_{\mathrm{f}^*}^2(\mathbf{x}^*) &= k(\mathbf{x}^*, \mathbf{x}^*) - \mathbf{K}(\mathbf{x}^*, \mathbf{X})\mathbf{K}(\mathbf{X}, \mathbf{X})^{-1}\mathbf{K}(\mathbf{x}^*, \mathbf{X})^T. \end{aligned} \tag{B.7}$$

References

[1] Y. Suzuki, D. G. Lignos, Fiber-based hysteretic model for simulating strength and stiffness deterioration of steel hollow structural section columns under cyclic loading, Earthquake Engineering and Structural Dynamics 49 (15) (2020) 1702–1720. doi:10.1002/eqe.3324.

[2] M. Wang, Y. Shi, Y. Wang, G. Shi, Numerical study on seismic behaviors of steel frame end-plate connections, Journal of Constructional Steel Research 90 (2013) 140–152. doi:10.1016/j.jcsr.2013.07.033.

[3] O. Muránsky, C. J. Hamelin, V. I. Patel, V. Luzin, C. Braham, The influence of constitutive material models on accumulated plastic strain in finite element weld analyses, International Journal of Solids and Structures 69-70 (2015) 518–530. doi:10.1016/j.ijsolstr.2015.04.032.

[4] M. Ohsaki, T. Miyamura, M. Kohiyama, M. Hori, H. Noguchi, H. Akiba, K. Kajiwara, T. Ine, High-precision finite element analysis of elastoplastic dynamic responses of super-high-rise steel frames, Earthquake Engineering and Structural Dynamics 38 (5) (2009) 635–654. doi:10.1002/eqe.900.

[5] T. Miyamura, T. Yamashita, H. Akiba, M. Ohsaki, Dynamic FE simulation of four-story steel frame modeled by solid elements and its validation using results of full-scale shake-table test, Earthquake Engineering and Structural Dynamics 44 (9) (2015) 1449–1469. doi:10.1002/eqe.2526.

[6] Y. Shi, M. Wang, Y. Wang, Experimental and constitutive model study of structural steel under cyclic loading, Journal of Constructional Steel Research 67 (8) (2011) 1185–1197. doi:10.1016/j.jcsr.2011.02.011.

[7] L. Xu, X. Nie, J. Fan, M. Tao, R. Ding, Cyclic hardening and softening behavior of the low yield point steel BLY160: Experimental response and constitutive modeling, International Journal of Plasticity 78 (2016) 44–63. doi:10.1016/j.ijplas.2015.10.009.

[8] U. Alper, T. Panos, Constitutive model for cyclic response of structural steels with yield plateau, Journal of Structural Engineering 137 (2) (2011) 195–206. doi:10.1061/(ASCE)ST.1943-541X.0000287.

[9] M. Ohsaki, T. Miyamura, J. Y. Zhang, A piecewise linear isotropic-kinematic hardening model with semi-implicit rules for cyclic loading and its parameter identification, Computer Modeling in Engineering & Sciences 111 (4) (2016) 303–333. doi:10.3970/cmes.2016.111.303.

[10] R. Hartloper Alexander, de Castro e Sousa Albano, G. Lignos Dimitrios, Constitutive modeling of structural steels: nonlinear isotropic/kinematic hardening material model and its calibration, Journal of Structural Engineering 147 (4) (2021) 04021031. doi:10.1061/(ASCE)ST.1943-541X.0002964.

[11] J. L. Chaboche, D. Nouailhas, Constitutive modeling of ratchetting effects–Part I: Experimental facts and properties of the classical models, Journal of Engineering Materials and Technology 111 (4) (1989) 384–392. doi:10.1115/1.3226484.

[12] S. Yamada, Y. Jiao, A concise hysteretic model of structural steel considering the Bauschinger effect, International Journal of Steel Structures 16 (3) (2016) 671–683. doi:10.1007/s13296-015-0134-9.

[13] A. Rusinek, R. Zaera, J. R. Klepaczko, Constitutive relations in 3-D for a wide range of strain rates and temperatures – Application to mild steels, International Journal of Solids and Structures 44 (17) (2007) 5611–5634. doi:10.1016/j.ijsolstr.2007.01.015.

[14] F. Yoshida, T. Uemori, K. Fujiwara, Elastic-plastic behavior of steel sheets under in-plane cyclic tension-compression at large strain, International Journal of Plasticity 18 (5) (2002) 633–659. doi:10.1016/S0749-6419(01)00049-3.

[15] S. Cooreman, D. Lecompte, H. Sol, J. Vantomme, D. Debruyne, Elasto-plastic material parameter identification by inverse methods: Calculation of the sensitivity matrix, International Journal of Solids and Structures 44 (13) (2007) 4329–4341. doi:10.1016/j.ijsolstr.2006.11.024.

[16] S. Koo, J. Han, K. P. Marimuthu, H. Lee, Determination of Chaboche combined hardening parameters with dual backstress for ratcheting evaluation of AISI 52100 bearing steel, International Journal of Fatigue 122 (2019) 152–163. doi:10.1016/j.ijfatigue.2019.01.009.

[17] S. K. Paul, S. Sivaprasad, S. Dhar, S. Tarafder, Key issues in cyclic plastic deformation: Experimentation, Mechanics of Materials 43 (11) (2011) 705–720. doi:10.1016/j.mechmat.2011.07.011.

[18] J. L. Beck, L. S. Katafygiotis, Updating models and their uncertainties. I: Bayesian statistical framework, Journal of Engineering Mechanics 124 (4) (1998) 455–461. doi:10.1061/(ASCE)0733-9399(1998)124:4(455).

[19] B. V. Rosić, A. Kučerová, J. Sýkora, O. Pajonk, A. Litvinenko, H. G. Matthies, Parameter identification in a probabilistic setting, Engineering Structures 50 (2013) 179–196. doi:10.1016/j.engstruct.2012.12.029.

[20] H. Rappel, L. A. A. Beex, L. Noels, S. P. A. Bordas, Identifying elastoplastic parameters with Bayes' theorem considering output error, input error and model uncertainty, Probabilistic Engineering Mechanics 55 (2019) 28–41. doi:10.1016/j.probengmech.2018.08.004.

[21] Y. Liu, L. Wang, K. Gu, M. Li, Artificial neural network (ANN) - Bayesian probability framework (BPF) based method of dynamic force reconstruction under multi-source uncertainties, Knowledge-Based Systems 237 (2022) 107796. doi:10.1016/j.knosys.2021.107796.

[22] Y. M. Marzouk, H. N. Najm, L. A. Rahn, Stochastic spectral methods for efficient Bayesian solution of inverse problems, Journal of Computational Physics 224 (2) (2007) 560–586. doi:10.1016/j.jcp.2006.10.010.

[23] J.-M. Marin, P. Pudlo, C. P. Robert, R. J. Ryder, Approximate Bayesian computational methods,

Statistics and Computing 22 (6) (2012) 1167–1180. doi:10.1007/s11222-011-9288-2.

[24] B. Do, M. Ohsaki, Bayesian optimization for inverse identification of cyclic constitutive law of structural steels from cyclic structural tests, Structures 38 (2022) 1079–1097. doi:10.1016/j.istruc.2022.02.054.

[25] G. Johansson, J. Ahlström, M. Ekh, Parameter identification and modeling of large ratcheting strains in carbon steel, Computers & Structures 84 (15) (2006) 1002–1011. doi:10.1016/j.compstruc.2006.02.016.

[26] B. M. Chaparro, S. Thuillier, L. F. Menezes, P. Y. Manach, J. V. Fernandes, Material parameters identification: Gradient-based, genetic and hybrid optimization algorithms, Computational Materials Science 44 (2) (2008) 339–346. doi:10.1016/j.commatsci.2008.03.028.

[27] A. H. Mahmoudi, S. M. Pezeshki-Najafabadi, H. Badnava, Parameter determination of Chaboche kinematic hardening model using a multi objective genetic algorithm, Computational Materials Science 50 (3) (2011) 1114–1122. doi:10.1016/j.commatsci.2010.11.010.

[28] R. de Carvalho, R. A. F. Valente, A. Andrade-Campos, Optimization strategies for non-linear material parameters identification in metal forming problems, Computers & Structures 89 (1) (2011) 246–255. doi:10.1016/j.compstruc.2010.10.002.

[29] A. Nath, K. K. Ray, S. V. Barai, Evaluation of ratcheting behaviour in cyclically stable steels through use of a combined kinematic-isotropic hardening rule and a genetic algorithm optimization technique, International Journal of Mechanical Sciences 152 (2019) 138–150. doi:10.1016/j.ijmecsci.2018.12.047.

[30] M. Benning, M. Burger, Modern regularization methods for inverse problems, Acta Numerica 27 (2018) 1–111. doi:10.1017/S0962492918000016.

[31] Y. Liu, L. Wang, A two-step weighting regularization method for stochastic excitation identification under multi-source uncertainties based on response superposition-decomposition principle, Mechanical Systems and Signal Processing 182 (2023) 109565. doi:10.1016/j.ymssp.2022.109565.

[32] A. Kaveh, A. Dadras, Structural damage identification using an enhanced thermal exchange optimization algorithm, Engineering Optimization 50 (3) (2018) 430–451. doi:10.1080/0305215X.2017.1318872.

[33] F. J. Montáns, F. Chinesta, R. Gómez-Bombarelli, J. N. Kutz, Data-driven modeling and learning in science and engineering, Comptes Rendus Mécanique 347 (11) (2019) 845–855. doi:10.1016/j.crme.2019.11.009.

[34] S. Arridge, P. Maass, O. Öktem, C.-B. Schönlieb, Solving inverse problems using data-driven models, Acta Numerica 28 (2019) 1–174. doi:10.1017/S0962492919000059.

[35] D. R. Jones, M. Schonlau, W. J. Welch, Efficient global optimization of expensive black-box functions, Journal of Global Optimization 13 (4) (1998) 455–492. doi:10.1023/A:1008306431147.

[36] B. Shahriari, K. Swersky, Z. Wang, R. P. Adams, N. de Freitas, Taking the human out of the loop: A review of Bayesian optimization, Proceedings of the IEEE 104 (1) (2016) 148–175. doi:10.1109/JPROC.2015.2494218.

[37] P. I. Frazier, A tutorial on Bayesian optimization, arXiv preprint (2018). arXiv:1807.02811.

[38] D. Systèmes, Abaqus User's Manual Ver. 2020 (2020).

[39] T. J. Santner, B. J. Williams, W. I. Notz, The design and analysis of computer experiments, 2nd Edition, Springer, New York, NY, 2018. doi:10.1007/978-1-4939-8847-1.

[40] J. Lemaitre, J.-L. Chaboche, Mechanics of solid materials, Cambridge University Press, 1994.

[41] E. Voce, The relationship between stress and strain for homogeneous deformation, Journal of the Institute of Metals 74 (1948) 537–562.

[42] J. L. Chaboche, G. Rousselier, On the plastic and viscoplastic constitutive equations–Part I: Rules developed with internal variable concept, Journal of Pressure Vessel Technology 105 (2) (1983) 153–158. doi:10.1115/1.3264257.

[43] P. J. Armstrong, C. O. Frederick, A mathematical representation of the multiaxial Bauschinger effect, Report RD/B/N731, Berkeley, UK (1966).

[44] C. E. Rasmussen, C. K. I. Williams, Gaussian processes for machine learning, The MIT Press, Cambridge, Massachusetts, 2006. doi:10.7551/mitpress/3206.001.0001.